Upscaling Methane Hydrate Dissociation Kinetic Model during Depressurisation

Junyu Yang [b, c], Qianghui Xu [a, c]*, Zhiying Liu [c], Lin Shi [c], Timan Lei [b] and Kai H. Luo [b]*

[a] School of Mechanical Engineering, Beijing Institute of Technology, Beijing 100081, China.

[b] Department of Mechanical Engineering, University College London, Torrington Place, London WC1E 7JE, United Kingdom.

[c] Key Laboratory for Thermal Science and Power Engineering of Ministry of Education, Department of Energy and Power Engineering, Tsinghua University, Beijing 100084, China.

* xuqh12@bit.edu.cn (Qianghui Xu)

* k.luo@ucl.ac.uk (Kai H. Luo)

Highlights

1. Pore-scale hydrate dissociation is simulated by the lattice Boltzmann method.
2. Effects of multiphase heat and mass transport on dissociation kinetics are clarified.
3. The representative-element-volume-scale kinetic model is upscaled and verified.
4. The effect of hydrate pore habits on the upscaled kinetic model is identified.

Abstract

In the present work, a pore-scale numerical simulation of methane hydrate dissociation by depressurisation is conducted to analyze the effect of heat and mass transfer on the dissociation rate for scaling up the kinetic model at the representative element volume (REV) scale. The mass transport limitation shows that the hydrate dissociation preferred to occur near the gas phase. The effective reaction surface area is introduced to measure the exposed hydrate surface to the gas phase during gas and water migration and is modelled as a function of local hydrate and water saturation and hydrate pore habits. Heat transport limitation is computed with the one-temperature model due to the local thermal equilibrium. Compared to the pore-scale simulation, the proposed REV-scale kinetic model predicts dissociation rates with a relative error of less than 10%, which is expected to increase the precision of the hydrate recovery forecast.

Keywords: methane hydrate, kinetic model, multiphase heat and mass transport, pore-scale simulation, lattice Boltzmann method

1. Introduction

Methane hydrate is the crystalline compound consisting of methane guest molecules inside the hydrogen-bonded water lattice (Sloan, 2003), which is regarded as a promising alternative energy resource due to its abundant deposits and high gas storage capacity (Chong et al., 2016). Typically, most hydrate resources are distributed in the deep marine sediment and terrestrial permafrost (Yu et al., 2021) under high-pressure and low-temperature conditions required for methane hydrate formation. In these sediments, methane hydrate occurred in various pore habits, such as grain-coating and pore-filling patterns (Ren et al., 2020), accompanied by gas-water multiphase flow in the complex pore structure. The extraction of methane hydrate is hindered by the extreme and diverse reservoir conditions, so methane hydrate development is still in its early stages among countries. The conventional exploitation techniques include thermal stimulation (Pang et al., 2009), depressurisation (Ji et al., 2001), inhibitor injection (Dong et al., 2009; Yuan et al., 2011) and their combinations (Wang et al., 2013). These methods facilitate hydrate dissociation by disrupting the thermodynamic equilibrium of the reservoir, and the depressurisation method is currently the most widely used. Since methane hydrate dissociation is a complicated multi-physical process involving multiphase heat and mass transport (Yin et al., 2016), the kinetic and transport properties of the reservoir can change dynamically during the exploitation, further limiting the recovery efficiency. A more comprehensive understanding of methane hydrate dissociation is still required to improve the methane hydrate exploitation technique.

In recent years, numerous efforts have been conducted to investigate the methane hydrate dissociation process (Chong et al., 2016; Cui et al., 2018; Song et al., 2014). Following the

rapid development of computational technology, numerical simulation has become an efficient method to evaluate production potential and optimise mining strategies of methane hydrate reservoirs (Anderson et al., 2011; Chen et al., 2018a; Feng et al., 2019). Most numerical solvers simulate methane hydrate production by calculating the mass and energy conservation equations with the dissociation reaction rate (Moridis, 2012). The dissociation reaction rate is determined by the kinetic model in these simulators at the representative element volume (REV) scale, which is essential for assuring forecast accuracy. For decades, extensive efforts have been made to obtain methane hydrate dissociation kinetics models. The most popular kinetic model currently in use is the Kim-Bishnoi model proposed by Kim et al. (Kim et al., 1987). This model characterises the intrinsic kinetic of methane hydrate dissociation. It attributed the reaction driving force to the methane fugacity difference between the reservoir and equilibrium state, with kinetic parameters obtained from stirred-tank reactor experiments. Based on the Kim-Bishnoi model, Jamaluddin et al. (Jamaluddin et al., 1989) simulated methane hydrate dissociation experiments by coupling the thermal effect. They found heat transport plays a significant role in the apparent dissociation rate. Youslf et al. (Youslf et al., 1991) conducted numerical and experimental investigations on the methane hydrate dissociation gas-water migration, emphasizing that mass transport significantly affects the apparent dissociation rate. The above investigations demonstrate the importance of heat and mass transport mechanisms in the kinetic model. In addition, since the methane hydrate sediment is typically porous media, the complex pore structure and diverse hydrate pore habits further influence the dissociation kinetic behaviour at the REV scale (Zhang et al., 2017). Although the methane hydrate dissociation kinetics model has received significant attention (Yin et al., 2016), it is still

challenging to accurately characterize the methane hydrate dissociation rate in the reservoir due to the multi-physical and multiphase mechanisms within diverse hydrate pore habits.

Different studies, from pore-scale to lab-scale, have been conducted to obtain a more accurate kinetic model. The typical lab-scale studies combined numerical and experimental approaches to obtain the kinetic parameters. Since the lab-scale simulators are also constructed at the REV scale (Song et al., 2018; Wang et al., 2018a; Wang et al., 2018b; Zhao et al., 2016), the kinetic model is usually derived by history matching (Yin et al., 2018). This data-based kinetic model lacked generalizability because it omitted the specific mechanisms of methane hydrate dissociation in sediment porous media. The pore-scale investigation is required in order to completely take into account the dissociation mechanisms in the pore structure. Various pore-scale experiments of two-dimensional microfluid visualization (Almenningen et al., 2018) provided some insights into the effect of multiphase heat and mass transport on the dissociation rate. With the rapid development of three-dimensional observation techniques such as magnetic resonance imaging (MRI) (Yang et al., 2017; Zhang et al., 2017) and microscopic X-ray computed tomography (micro-CT) (Yang et al., 2016), it was found that gas-water migration and interphase mass transport of methane molecules play a significant role in the dissociation dynamics. The complicated heat and mass transport within the multiphase system are fully coupled and alter the thermodynamic conditions in the sediment, thereby affecting the dissociation rate. In addition, some pore-scale numerical studies were performed to further elucidate the dissociation mechanisms behind the experimental observation (Song et al., 2021; Wang et al., 2019; Yang et al., 2021b; Zhang et al., 2019). However, it is challenging to scale up the kinetic model while fully taking into account the controlling mechanisms from the pore-

scale perspectives. Yu et al. (Yu et al., 2017) proposed the kinetic model of methane hydrate dissociation using a pore-scale simulation. They conducted upscaling work, considering the single-phase flow with heat and mass transport during the dissociation process. However, this kinetic model failed to consider the effect of complicated multiphase flow and interfacial transport on the dissociation rate. With pore-scale multiphase dissociation simulation, our recent work (Yang et al., 2021b) identified that the interfacial mass transport of methane molecules significantly influenced the dissociation rate. We also suggested a modified kinetic model to account for the mass transport effect by the water layer thickness. However, the simulation was restricted in a single pore throat. Subsequently, we conducted numerical investigations on the dissociation process in more complicated pore structures to recognise the influence of heat and mass transport mechanisms (Yang et al., 2022b), but a quantitative analysis about the influence of these mechanisms on the apparent kinetics is still lacking. Therefore, more work is still required to scale up the kinetic model by considering the complex multiphase distribution and various hydrate pore habits in the sediment based on pore-scale physics.

The objective of the present work is to upscale the kinetic model from the pore-scale perspective to comprehensively describe the methane hydrate dissociation rate in REV, considering multiphase heat and mass transport mechanisms within different hydrate sediment pore structures. A pore-scale numerical model with the lattice Boltzmann (LB) method is used to simulate the methane hydrate dissociation process during depressurisation. The pore-scale numerical results identify the critical physical mechanisms affecting the methane hydrate dissociation rate, and experimental observations are demonstrated to corroborate the results.

The REV-scale kinetic model is derived and carefully verified based on pore-scale physics. Different methane hydrate pore habits and gas-water distributions are investigated to ensure the applicability of the proposed kinetic model. The present work aims to provide a more accurate kinetic model for production forecast and enlighten the ideas for methane hydrate upscaling research. In what follows, a brief introduction of the physical problem, pore-scale modelling, REV-scale modeling, and upscaling method will be presented in Section 2. After understanding the pore-scale heat and mass transport mechanisms during methane hydrate dissociation in Section 3.1, the upscaled kinetic model and its validation will be introduced in Sections 3.2 and 3.3.

2. Numerical method

2.1. Physical description of hydrate dissociation

Methane hydrate dissociation by depressurisation is complicated due to multiple physicochemical processes in the pore structure, which is schematically demonstrated in Fig. S1 (Yang et al., 2022b). Dissociation reaction occurs on the methane hydrate surface when the methane hydrate phase equilibrium is broken due to the pressure decrease. The multiphase flow dynamics in the sediment are impacted by the formation of gas and water as hydrate structures melt, changing the relative permeability of the sediment. On the water-covered hydrate surfaces, the released methane molecules need to transport through the water layer into the gas phase via gas diffusion (Wang et al., 2019; Yang et al., 2016). The complicated multiphase flow and interfacial mass transport influence the methane fugacity (concentration) evolution in the pore structure. Meanwhile, the reaction heat absorption due to the endothermic hydrate dissociation leads to the temperature decrease through the conjugate heat transport between phases. The

multiphase flow, heat and mass transport with phase transition are fully coupled to determine the thermodynamic condition in the sediment, which in turn influences the dissociation rate.

To construct the mathematical description of the dissociation process for the numerical model, major assumptions and simplifications in the present work include the following: (1) methane molecules can be dissolved in the water as a dilute solution, and the gas phase is regarded as an ideal gas; (2) the dissociation reaction only occurs at the hydrate surface; (3) influences of heat and mass transport on gas-water multiphase flow can be neglected; (4) since the temperature variation is not dramatic, the physical properties can be treated as constant. Based on the above assumptions, governing equations of multiphase fluid flow, methane molecule mass transport and conjugate heat transport can be written as (Yang et al., 2022b)

$$\frac{\partial \rho^{\sigma}}{\partial t}+\nabla\cdot\left(\rho^{\sigma}\mathbf{u}\right)=0 \tag{1}$$

$$\begin{aligned}\frac{\partial\left(\rho^{\sigma}\mathbf{u}^{\sigma}\right)}{\partial t}+\nabla\cdot\left(\rho^{\sigma}\mathbf{u}^{\sigma}\mathbf{u}^{\sigma}\right)=&-\nabla p+\nabla\cdot\left(\rho^{\sigma}\upsilon^{\sigma}\left(\nabla\mathbf{u}^{\sigma}+\left(\nabla\mathbf{u}^{\sigma}\right)^{T}\right)\right)\\&+\nabla\left(\rho^{\sigma}\left(\xi^{\sigma}-\frac{2}{3}\upsilon^{\sigma}\right)\left(\nabla\cdot\mathbf{u}^{\sigma}\right)\right)+\mathbf{F}\end{aligned} \tag{2}$$

$$\frac{\partial C_{\sigma}}{\partial t}+\nabla\cdot\left(C_{\sigma}\mathbf{u}^{\sigma}\right)=D_{\sigma}\nabla^{2}C_{\sigma} \tag{3}$$

$$\rho c_{p}\frac{\partial T}{\partial t}+\nabla\cdot\left(\rho c_{p}T\mathbf{u}\right)=\nabla\cdot\left(\lambda\nabla T\right)+S_{R} \tag{4}$$

where the superscript or subscript σ denotes physical properties in each phase ($\sigma=\mathrm{w}$ for the water phase and $\sigma=\mathrm{g}$ for the gas phase). ρ is the fluid density and $\mathbf{u}$ is the velocity. p, υ and ξ are the pressure, kinematic viscosity and bulk viscosity, respectively. C and T represents the methane concentration and temperature, respectively. D is the diffusivity, c_p is the heat capacity, and λ is the thermal conductivity. S_R is the heat source term. At the gas-water interface, mass conservation and species conservation write (Maes and Soulaine,

2018)

$$\rho^{\mathrm{w}}\left(\mathbf{u}^{\mathrm{w}}-\mathbf{w}\right)\cdot\mathbf{n}_{\mathrm{wg}}=\rho^{\mathrm{g}}\left(\mathbf{u}^{\mathrm{g}}-\mathbf{w}\right)\cdot\mathbf{n}_{\mathrm{wg}} \tag{5}$$

$$\begin{gathered}\left(C_{\mathrm{w}}\left(\mathbf{u}^{\mathrm{w}}-\mathbf{w}\right)-D_{\mathrm{w}}\nabla C_{\mathrm{w}}\right)\cdot\mathbf{n}_{\mathrm{wg}}=\left(C_{\mathrm{g}}\left(\mathbf{u}_{\mathrm{g}}-\mathbf{w}\right)-D_{\mathrm{g}}\nabla C_{\mathrm{g}}\right)\cdot\mathbf{n}_{\mathrm{wg}}\\ C_{\mathrm{w}}=HC_{\mathrm{g}}\end{gathered} \tag{6}$$

where $\mathbf{w}$ is the velocity of the interface and $\mathbf{n}_{\mathrm{wg}}$ is the normal vector to the interface. H is the Henry coefficient for Henry's law. At the hydrate surface, dissociation occurs as

$$\mathrm{CH_4}\cdot N_{\mathrm{H}}\mathrm{H_2O}\rightarrow\mathrm{CH_4}+N_{\mathrm{H}}\mathrm{H_2O},\ \Delta H>0 \tag{7}$$

where N_{H} is the hydrate number set as $N_{\mathrm{H}}=6$ in the present work. ΔH is the reaction enthalpy. The intrinsic kinetic is computed using the Kim-Bishnoi model (Kim et al., 1987) as

$$\frac{dn_{\mathrm{CH_4}}}{dt}=k_0\exp\left(\frac{E_A}{RT}\right)\left(f_{\mathrm{eq}}-f\right)A_{\mathrm{s}} \tag{8}$$

where k_0, E_A and A_{s} represent the pre-exponential factor, activation energy and reaction surface area, respectively. Based on the assumption of an ideal gas and dilute solution, the methane fugacity f can be characterised by the methane concentration in the gas or water phase, i.e. C_{g} and C_{w}. Since the concentration follows Henry's law by $C_{\mathrm{w}}=HC_{\mathrm{g}}$, the reaction mass flux at the hydrate surface Π can be obtained by

$$\Pi=-k_{\mathrm{g}}\exp\left(\frac{E_A}{RT}\right)\left(C_{\mathrm{eq,\,g}}-C_{\mathrm{g}}\right)_{\mathrm{h}}=-k_{\mathrm{w}}\exp\left(\frac{E_A}{RT}\right)\left(C_{\mathrm{eq,\,w}}-C_{\mathrm{w}}\right)_{\mathrm{h}} \tag{9}$$

where k_{g} and k_{w} conform to $k_{\mathrm{w}}=k_{\mathrm{g}}/H$. Inspired by the Kamath model (Kamath, 1984; Moridis, 2012), the equilibrium concentration can be calculated by

$$C_{\mathrm{eq,\,w}}=HC_{\mathrm{eq,\,g}}=H\exp\left(33.12-\frac{9005.5}{T}\right)\ (\mathrm{mol/L}),\ 273.15\ \mathrm{K}<T\le 298.15\ \mathrm{K} \tag{10}$$

More details about the model setting of the dissociation intrinsic kinetic and hydrate phase equilibrium condition can be found in our previous work (Yang et al., 2021b; Yang et al.,

2022b).

2.2 Pore-scale modelling

Pore-scale modelling of methane hydrate dissociation in the sediment porous media within REV is performed to understand the heat and transport mechanisms and develop a more precise kinetic model for REV-scale simulators. The numerical models and configurations in the present work are introduced in this section.

2.2.1 Simulation configuration

Based on the governing equations (1)-(10), pore-scale numerical modelling is conducted within the multiphase system in the sediment pore structure. To consider the impact of various hydrate pore habits on the dissociation kinetics, two typical hydrate distributions including pore-filling (PF) and grain-coating (GC) are introduced in the numerical simulation with different hydrate saturations, as shown in Fig. 1. GCh and PFh represent two heterogeneous hydrate distribution. The black colour represents the sand in the sediment with the grain diameter $d = 300\ \mu\text{m}$, and the grey colour indicates the methane hydrate. The size of each porous structure for pore-scale modelling is $3\ \text{mm} \times 6\ \text{mm}$ with the porosity of $\phi_{\text{por}} = 0.48$, which is regarded as an independent REV.

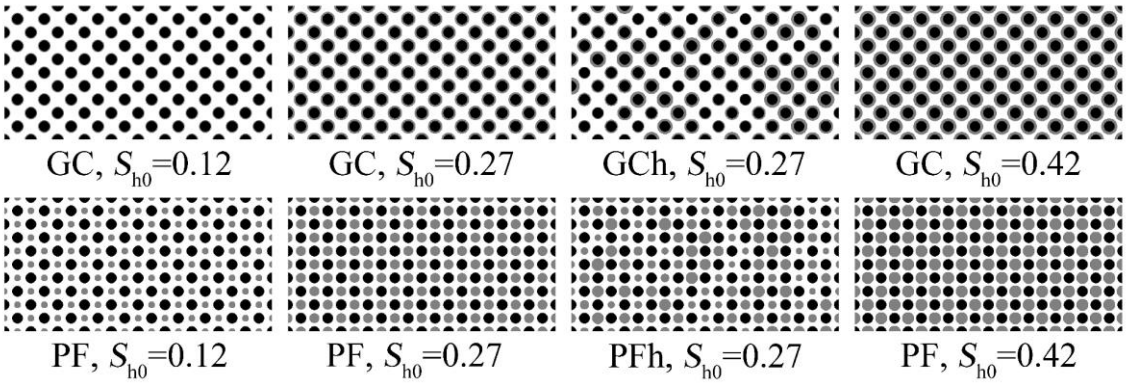

Fig. 1. Different hydrate structures in the sediment used for simulations. The black colour

represents sands, and the grey colour denotes hydrate.

This work focuses on the kinetic behaviour under various multiphase heat and mass transport conditions, and different water saturations are used in the simulations to look into the multiphase effect. The distribution of gas and water is set randomly for each case, and Fig. 2 gives examples of the gas-water distributions with different water saturations placed in the sediment pore structure of GC, $S_{h0} = 0.27$. The saturations of hydrate, water, and gas satisfy

$$S_h + S_w + S_g = 1 \tag{11}$$

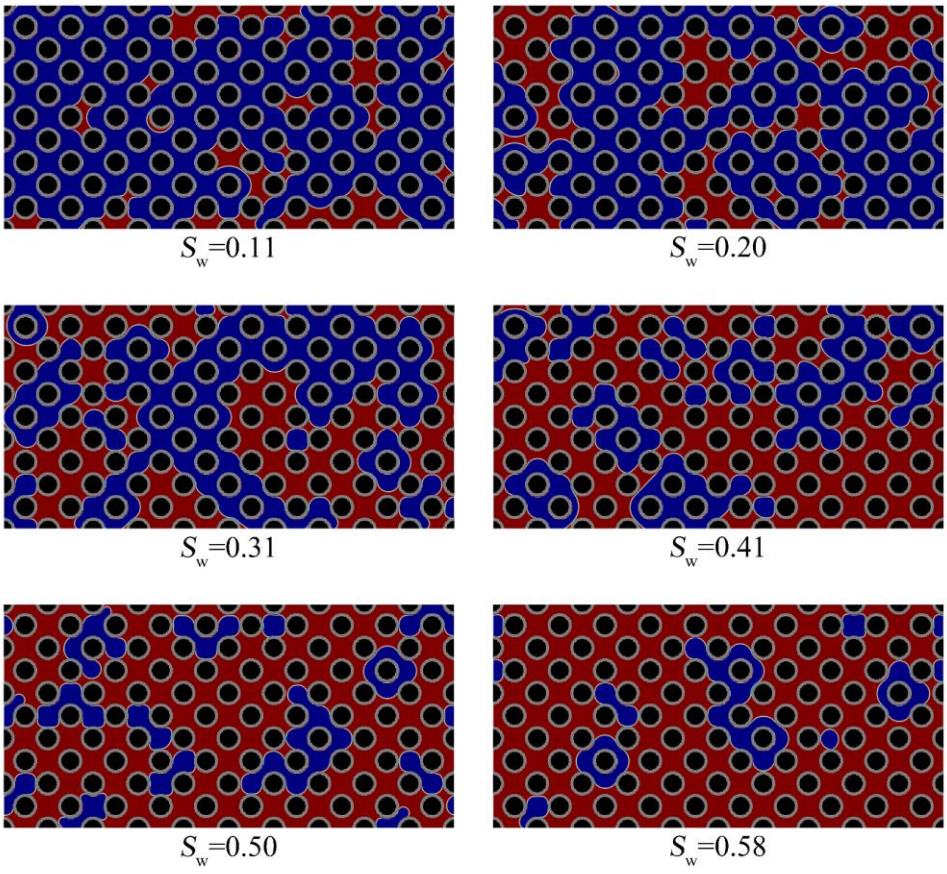

Fig. 2. Initial gas-water multiphase distribution in simulations. The red colour represents water, and the blue is gas.

At the initial stage of the simulation, gas, water, and hydrate are in equilibrium at the initial temperature $T_0 = 288.15$ K with the gaseous methane concentration of the equilibrium

value $C_g = 6.5$ mol/L by Eq. (10), which is close to the marine hydrate sediment conditions (Niu et al., 2021). Then, the methane concentration in the gas phase is artificially shifted to a low value $C_g = 2.0$ mol/L to trigger depressurisation. The main physical properties used in the simulation are listed in Table 1. In most marine hydrate sediment, the pressure is typically very high, above 10 MPa (Niu et al., 2021), resulting in high gas density in the reservoir. Therefore, a relatively high gas density $\rho_g = 110$ kg/m^3 is adopted in the simulation. The Henry coefficient and diffusivity in the water phase are set to a small value $H = 0.2$ and $D_w = 1.0\times10^{-8}$ m^2/s, to mimic the low solubility and low diffusivity of methane in water. Other parameters including the intrinsic kinetic parameters and thermal properties are obtained based on the previous work (Wang et al., 2018c; Yu et al., 2017; Zhang et al., 2019).

Table 1. Physical properties in the simulations

Water density, ρ_{w0}	1000 kg/m^3
Gas density, ρ_{g0}	110 kg/m^3
Initial temperature, T_0	288.15 K
Initial concentration in gas phase, C_{g0}	6.5 mol/L
Henry coefficient, H	0.2
Kinematic viscosity of water, υ_w	1.0×10^{-6} m^2/s
Kinematic viscosity of gas, υ_g	1.0×10^{-7} m^2/s
Methane diffusivity in water, D_w	1.0×10^{-8} m^2/s
Methane diffusivity in gas, D_g	1.0×10^{-6} m^2/s
Pre-exponential factor, k_g	5.13×10^{9} m/s
Activation energy, E_A / R	9399 K

Reaction enthalpy, ΔH	51.86 kJ/mol
Thermal conductivity of water, λ_{w}	0.55 W/(m·K)
Thermal conductivity of gas, λ_{g}	0.045 W/(m·K)
Thermal conductivity of hydrate, λ_{h}	0.49 W/(m·K)
Thermal conductivity of sand, λ_{s}	0.90 W/(m·K)
Specific heat capacity of water, $c_{p\mathrm{w}}$	4.2 kJ/(kg·K)
Specific heat capacity of gas, $c_{p\mathrm{g}}$	3.0 kJ/(kg·K)
Specific heat capacity of hydrate, $c_{p\mathrm{h}}$	2.1×10^{3} kJ/(m^3·K)
Specific heat capacity of sand, $c_{p\mathrm{s}}$	2.0×10^{3} kJ/(m^3·K)

2.2.2 Lattice Boltzmann method

The lattice Boltzmann (LB) method (Krüger et al., 2017), which is discretized from the Boltzmann equation with the approximation of the collision operator, is adopted to simulate the methane hydrate dissociation process in the present work. The numerical models are briefly introduced in this section, including multiphase flow, interfacial mass transport, conjugate heat transport, and heterogeneous dissociation reaction with structure evolution. More details and validations of the models can be found in our previous work (Yang et al., 2022a; Yang et al., 2021a).

2.2.2.1 Multiphase flow model

The pseudopotential model is adopted in the present work to simulate the gas-water multiphase flow described by Eq. (1) and (2). The LB equation for the σth (σ=w or g) component with the multiple-relaxation-time (MRT) collision operator is expressed as

$$\begin{aligned}\mathbf{f}^{\sigma}(\mathbf{x}+\mathbf{c}_i\Delta t,t+\Delta t)-\mathbf{f}^{\sigma}(\mathbf{x},t)=&-\mathbf{M}^{-1}\mathbf{S}^{\sigma}\left[\mathbf{m}^{\sigma}(\mathbf{x},t)-\mathbf{m}^{\sigma,\mathrm{eq}}(\mathbf{x},t)\right]\\&+\Delta t\cdot\mathbf{M}^{-1}\left(\mathbf{I}-\frac{\mathbf{S}^{\sigma}}{2}\right)\mathbf{F}^{\sigma}+\mathbf{w}S_M^{\sigma}\end{aligned}\tag{12}$$

where $\mathbf{f}^{\sigma}=\left(f_0^{\sigma},f_1^{\sigma},...,f_{q-1}^{\sigma}\right)^T$ is the density distribution function and $\mathbf{M}$ is the transformation matrix converting the velocity space to the moment space as $\mathbf{m}^{\sigma}=\mathbf{M}\mathbf{f}^{\sigma}$. A two-dimensional nine-velocity (D2Q9) lattice model (Krüger et al., 2017) is used with the definition of relaxation matrix $\mathbf{S}^{\sigma}=\mathrm{diag}\left(0,\omega_e^{\sigma},\omega_{\varepsilon}^{\sigma},0,\omega_q^{\sigma},0,\omega_q^{\sigma},\omega_{\upsilon}^{\sigma},\omega_{\upsilon}^{\sigma}\right)$, where $\omega_{\upsilon}^{\sigma}$ is related to the kinematic viscosity by $\upsilon^{\sigma}=\left(1/\omega_{\upsilon}^{\sigma}-0.5\right)\Delta t/3$. The fluid density and velocity of the σth component can be calculated by

$$\rho^{\sigma}=\sum f_i^{\sigma},\ \rho^{\sigma}\mathbf{u}^{\sigma}=\sum f_i^{\sigma}\mathbf{e}_i+\frac{\Delta t}{2}\mathbf{F}^{\sigma},\tag{13}$$

and the total density and velocity are

$$\rho=\sum\rho^{\sigma},\ \mathbf{u}=\sum\rho^{\sigma}\mathbf{u}^{\sigma}/\sum\rho^{\sigma}.\tag{14}$$

In the present work, both intracomponent interaction force $\mathbf{F}_{\sigma\sigma}$ and intercomponent interaction force $\mathbf{F}_{\sigma\bar{\sigma}}$ are introduced to realize multicomponent phase separation with large density ratios as

$$\begin{aligned}\mathbf{F}_{\sigma\sigma}&=-G_{\sigma\sigma}\psi_{\sigma}(\mathbf{x})\sum_{\alpha}w\left(\left|\mathbf{e}_{\alpha}\right|^2\right)\psi_{\sigma}(\mathbf{x}+\mathbf{e}_{\alpha})\mathbf{e}_{\alpha},\\\mathbf{F}_{\sigma\bar{\sigma}}&=-G_{\sigma\bar{\sigma}}\varphi_{\sigma}(\mathbf{x})\sum_{\alpha}w\left(\left|\mathbf{e}_{\alpha}\right|^2\right)\varphi_{\bar{\sigma}}(\mathbf{x}+\mathbf{e}_{\alpha})\mathbf{e}_{\alpha}\end{aligned}\tag{15}$$

where ψ_{σ} and φ_{σ} are the fluid potentials of water and gas, and their definition can be found in ref. (Yang et al., 2022a). Assuming that the gas phase is an ideal gas, the intracomponent force of the gas component $\mathbf{F}_{\mathrm{gg}}$ is set as zero. The phase fraction of water x_{w} can be defined as

$$x_{\mathrm{w}}=\frac{\varphi_{\mathrm{w}}}{\varphi_{\mathrm{w}}+\varphi_{\mathrm{g}}}\tag{16}$$

2.2.2.2 Interfacial mass transport model

The CST-LB model (Yang et al., 2021a) in the D2Q5 scheme is adopted to compute the interfacial mass transport of methane molecules. The CST-LB equation is written as

$$g_\alpha(\mathbf{x}+\mathbf{e}_\alpha\Delta t, t+\Delta t)-g_\alpha(\mathbf{x},t)=-\frac{1}{\tau_D}[g_\alpha(\mathbf{x},t)-g_\alpha^{\mathrm{eq}}(\mathbf{x},t)]+\Omega_{\mathrm{CST},\alpha} \tag{17}$$

where g_α is the concentration distribution function. The effective diffusion coefficient and the total methane concentration can be calculated by

$$C=x_{\mathrm{w}}C_{\mathrm{w}}+(1-x_{\mathrm{w}})C_{\mathrm{g}}=\sum_\alpha g_\alpha \tag{18}$$

$$D=\frac{D_{\mathrm{w}}D_{\mathrm{g}}}{x_{\mathrm{w}}D_{\mathrm{w}}+(1-x_{\mathrm{w}})D_{\mathrm{g}}}=\frac{1}{2}(1-J_0)(\tau_D-0.5)\frac{\Delta x^2}{\Delta t} \tag{19}$$

$\Omega_{\mathrm{CST},\alpha}$ is the CST collision term to calculate the concentration jump at the interface decided by Henry's law, which is written as

$$\Omega_{\mathrm{CST},\alpha}=\left(1-\frac{1}{2\tau_D}\right)J_\alpha C\frac{H-1}{Hx_{\mathrm{w}}+(1-x_{\mathrm{w}})}(\mathbf{e}_\alpha\cdot\nabla x_{\mathrm{w}})\Delta t \tag{20}$$

At the hydrate surface, heterogeneous chemical reaction boundary treatment (Yang et al., 2022a) is enforced as

$$\mathbf{e}_\alpha g_\alpha(\mathbf{x},t)=-\mathbf{e}_{\bar{\alpha}}g_{\bar{\alpha}}^*(\mathbf{x},t)+\Pi \tag{21}$$

where the unknown concentration distribution function g_α is computed using the dissociation reaction mass flux Π and post-collision distribution function in the opposite direction of α, $g_{\bar{\alpha}}^*$.

2.2.2.3 Conjugate heat transport model

The double-distribution-function thermal LB model (He et al., 2019) in the D2Q5 framework is used to simulate the conjugate heat transport in the sediment as

$$h_\alpha(\mathbf{x}+\mathbf{e}_\alpha\Delta t, t+\Delta t)-h_\alpha(\mathbf{x},t)=-\frac{1}{\tau_\chi}[h_\alpha(\mathbf{x},t)-h_\alpha^{\mathrm{eq}}(\mathbf{x},t)]+J_\alpha S_c\Delta t+J_\alpha S_r\Delta t \tag{22}$$

where h_α is the temperature distribution function. The thermal diffusivity χ is computed by

$$\chi = \frac{\lambda}{\rho c_p} = \frac{1}{2}\left(1 - J_0\right)\left(\tau_\chi - 0.5\right)\frac{\Delta x^2}{\Delta t} \tag{23}$$

S_r is the dissociation reaction heat source computed by the reaction enthalpy ΔH and S_c is the conjugate source term which is computed by

$$S_c = \nabla\left(\frac{1}{\rho c_p}\right)\cdot\left(-\lambda\nabla T + \rho c_p T\mathbf{u}\right) \tag{24}$$

2.2.2.4 Hydrate structure evolution model

The volume of pixel (VOP) method (Kang et al., 2006) is employed in the present work to track the hydrate structure evolution by updating the hydrate volume of each node as

$$V_{\mathrm{hdy}}\left(t + \Delta t\right) = V_{\mathrm{hdy}}\left(t\right) - \Pi V_{\mathrm{M}} A_{\mathrm{s}} \Delta t \tag{25}$$

where V_{M} is the molar volume of the methane hydrate. When the hydrate volume declines to zero, the hydrate node is converted into a fluid node. The physical properties at the converted node are then updated by averaging over the adjacent fluid nodes.

The above LB models are capable of solving the governing equations (1)-(10) (Guo et al., 2022; Karani and Huber, 2015; Yang et al., 2021a) and the numerical procedure is schematically illustrated in Fig. S2 as our previous work (Yang et al., 2022b).

2.3 REV-scale models

In the REV-scale modelling, the mass and energy equations within a REV can be written as (Moridis, 2012)

$$\frac{d}{dt}\int_{V_{\mathrm{REV}}} M dV = \int_{\Gamma_{\mathrm{REV}}} \mathbf{Q}\cdot\mathbf{n} dA + \int_{V_{\mathrm{REV}}} S dV \tag{26}$$

where M, $\mathbf{Q}$ and S are the accumulation term, flux term, and source term respectively.

V_{REV} and Γ_{REV} are the volume and surface area of the REV. For the mass equation of methane,

$$M = \sum_{i=\mathrm{w,\,g}} \phi_{\mathrm{por}} S_i \bar{C}_i,\ \mathbf{Q} = \sum_{i=\mathrm{w,\,g}} -\frac{K_i}{\mu_i}\nabla p\bar{C}_i - \tilde{D}_i \nabla \bar{C}_i,\ S = \dot{r} \tag{27}$$

where $\bar{C}$ is the phase-averaged concentration of methane, K is the permeability, $\tilde{D}_{\mathrm{i}}$ is the effective diffusivity at the surface of REV, and $\dot{r}$ is the dissociation reaction rate. For the energy equation, a one-temperature model based on the local thermal equilibrium assumption is typically adopted as

$$\begin{aligned} M &= \sum_{i=\mathrm{g,w,h}} S_i \rho_i c_{pi} \phi_{\mathrm{por}} \bar{T} + \rho_{\mathrm{s}} c_{ps}\left(1-\phi_{\mathrm{por}}\right)\bar{T}, \\ \mathbf{Q} &= -\tilde{\lambda}\nabla \bar{T} + \sum_{i=\mathrm{g,w}} \rho_i c_{pi} \bar{T}\left(-\frac{K_i}{\mu_i}\nabla p\right),\ S = \dot{r}\Delta H \end{aligned} \tag{28}$$

where $\bar{T}$ is the volume-average temperature, $\tilde{\lambda}$ is the effective thermal conductivity at the surface of REV. The dissociation reaction rate $\dot{r}$ is provided by (Kim et al., 1987)

$$\dot{r} = \tilde{k}_0 \exp\left(\frac{E_{\mathrm{A}}}{R\bar{T}}\right) F_A A_{\mathrm{s}}\left(\bar{f} - \bar{f}_{eq}\right) \tag{29}$$

where $\tilde{k}_0$ is the apparent pre-exponential factor at the REV scale, F_A is the area adjustment factor, A_{s} is the hydrate surface area in the REV and $\bar{f}$ is the phase-average fugacity.

Even though the REV-scale dissociation rate equation (Eq. (29)) shares a similar format as the pore-scale dissociation rate equation (Eq. (8)), two variations were introduced during upscaling. Firstly, at the REV scale, all the physical variables, including the temperature and component fugacity, are averaged over the control volume and derived by Eq. (26)-(28). Secondly, as inspired by the previous work (Yang et al., 2021b; Yin et al., 2018), the apparent pre-exponential factor $\tilde{k}_0$ and area adjustment factor F_A can be introduced to account for the effects of pore-scale heat and mass transport on the REV-scale dissociation rate.

Mathematically, the $\tilde{k}_0$ and F_A depend on each other and should be taken into account together. As reviewed, the relation of the pre-exponential factor between the pore-scale and REV-scale model should be further clarified when considering the effect of the gas-water migration and hydrate pore habits (Yang et al., 2021b). Instead of the "unphysical" data fitting to yield the area adjustment factor F_A, the present study quantifies the factor via an upscaling investigation based on pore-scale hydrate dissociation mechanisms.

2.4 Upscaling conception of the kinetic model

The upscaling concept of methane hydrate dissociation by depressurisation from the pore scale to the REV scale is presented graphically in Fig. 3. From the REV-scale perspective, as shown on the left side of Fig. 3, the hydrate field can be discretized numerous control volumes with each control volume containing a homogeneous mixture consisting of gas, water, sand, and hydrate. At the pore scale, the heterogeneous gas-water phase distribution and hydrate pore habits, including grain-coating and pore-filling patterns can be explicitly described in each control volume (Fukumoto et al., 2018), as shown on the right side of Fig. 3. As the previous work (Yin et al., 2016), a reliable REV-scale kinetic model for the methane hydrate dissociation should be developed by comprehensively coupling the heat and mass transport as well as the dissociation kinetics described by Eqs. (26)-(29), not just limited to the single dissociate rate equation as Eq. (29). According to Eq. (26), accurate calculations of the REV-scale flux and source terms are crucial to achieving accurate hydrate field production forecasts. For the flux term, the permeability model has received extensive attention via pore-scale investigations (Chen et al., 2018b; Zhang et al., 2020). In contrast, as for source terms, the upscaling work for a more accurate REV-scale dissociation rate model is still limited. Therefore, the upscaling

principle in the present work is to derive the value or submodel for the apparent pre-exponential factor $\tilde{k}_0$ and area adjustment factor F_A by quantifying the effects of heat and mass transfer on the hydrate dissociation rate through a series of numerical simulations with different pore habits (Fig. 1), phase distributions (Fig. 2), fluid flow rates and thermal conditions, so that the REV-scale kinetic model of Eqs. (26)-(29) can be closed.

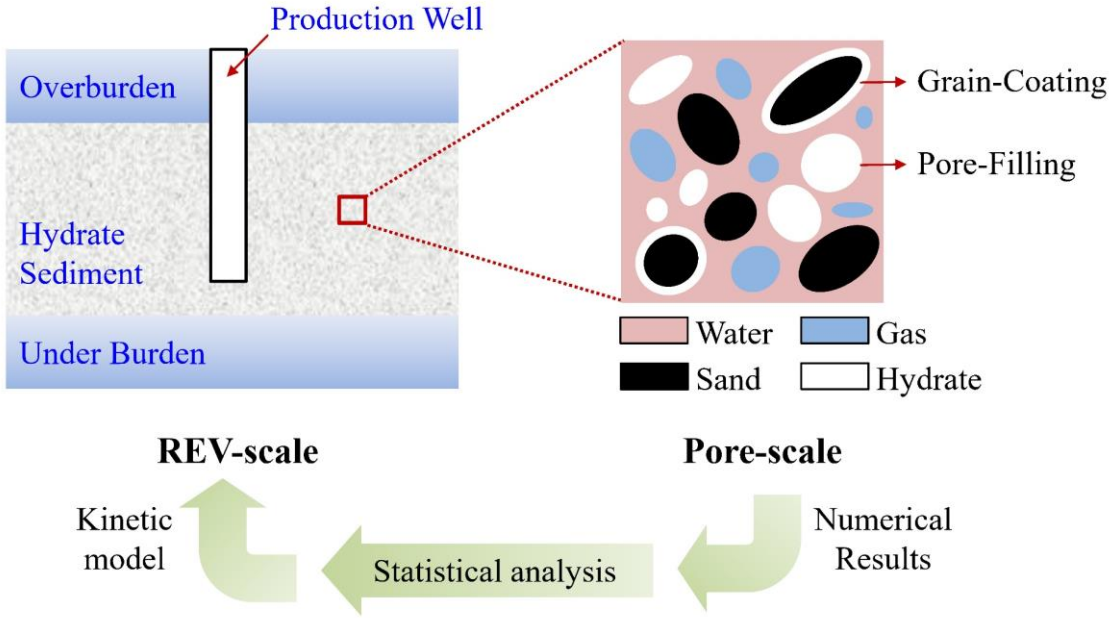

Fig. 3. Graphical presentation of upscaling concept.

To highlight the kinetic model in the source term S in Eq. (26), we assume that the gradient of adjacent REV conditions is not substantial in the flow direction because, as shown in Fig. 1, the computational domain for pore-scale modelling, which serves as the REV, is much smaller than the field scale and locates far away from the production/injection well. Therefore, periodic boundaries are used at the left and right sides of the computational domain, while the top and bottom are the walls with no mass and heat fluxes. Gas-water multiphase flow with various velocities is driven by numerical body forces in the horizontal direction. With this setting, interference of the flux term $\mathbf{Q}$ can be eliminated to facilitate the investigation of the

kinetic model. More details on the upscaling work will be introduced in Section 3.2.

3. Results and Discussions

In the present study, methane hydrate dissociation under different water saturations and fluid flow rates is firstly analysed to understand the role of multiphase heat and mass transport in the REV-scale dissociation kinetics. Based on the pore-scale dissociation mechanism, the methane hydrate dissociation kinetic model is then upscaled and verified. Hydrate dissociation within various sediment structures is also compared to figure out the effect of methane hydrate pore habits on the upscaled kinetic model.

3.1 Methane hydrate dissociation mechanisms

3.1.1 Methane hydrate dissociation under isothermal conditions

Methane hydrate dissociation under isothermal conditions without considering reaction thermal effect is firstly analysed to highlight the role of multiphase mass transport. Dissociation processes under different water saturations and fluid flow rates are investigated. The fluid velocity is characterised by the Péclet number as

$$\mathrm{Pe} = \frac{Ud}{D_{\mathrm{w}}} \tag{30}$$

where U is Darcy velocity. Two typical fluid velocities are adopted in the simulation, including high Pe ($\mathrm{Pe} \sim O(0.01)$) and low Pe ($\mathrm{Pe} \sim O(1)$), to represent situations of the near-well high flow rate zone and far-well low flow rate zone. In this section, the GC sediment of $S_{\mathrm{h0}} = 0.27$ is employed for the numerical analyses.

Fig.4 compares the hydrate conversion ratio curves under different water saturations and fluid velocities, which are computed by dividing dissolved hydrate volume over the original

hydrate volume as $1-S_{\mathrm{h}}(t)/S_{\mathrm{h0}}$. The curve shows that the dissociation rate decreases with time, and the change of conversion ratio is already very slow at 20 s. Therefore, we focus on the numerical results before 20 s. As the water saturation increases, the methane hydrate dissociation rate declines significantly, indicating the presence of water limits the dissociation process. For the same sediment water saturation, the dissociation rate under the high Pe condition is higher than low Pe, especially when water saturation is high ($S_{\mathrm{w}}>0.3$). For a more intuitive explanation of the above phenomenon, the evolution of methane concentration and hydrate distribution for different Pe under a typical low water saturation $S_{\mathrm{w}}=0.20$ is first illustrated in Fig. 5. Generally, numerical results show the methane concentration in gas C_{g} remains almost uniform and much higher than C_{w} due to the high gas diffusivity D_{g} and low Henry coefficient H. Therefore, to highlight the concentration distribution in the water phase for a more explicit discussion, the concentration in the gas phase is not displayed but is replaced by navy blue to distinguish the phase distribution.

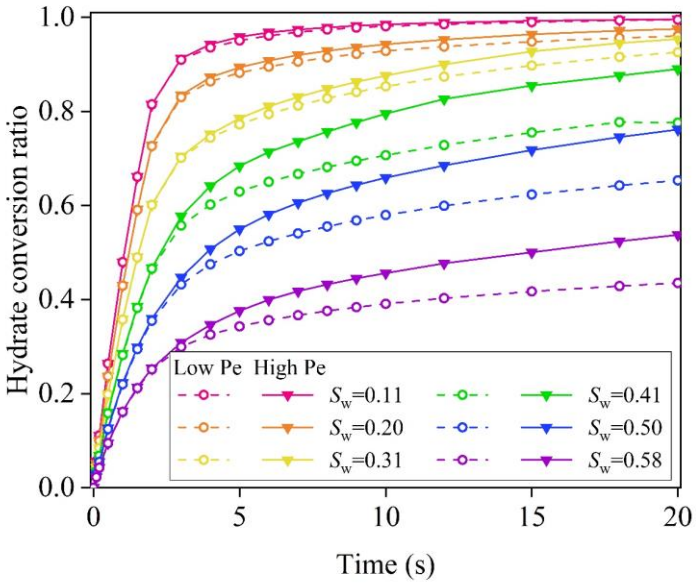

Fig. 4. Comparison of isothermal hydrate conversion ratio curves under different S_{w} and

Pe.

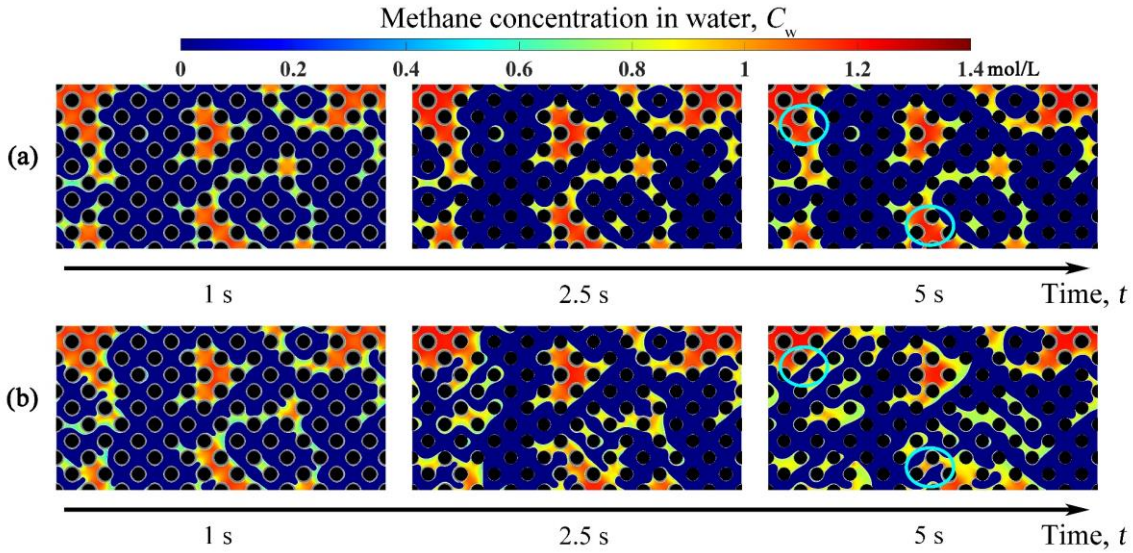

Fig. 5. The temporal evolution of methane concentration in water during methane hydrate dissociation in the GC sediment of $S_w = 0.20$ and $S_{h0} = 0.27$ at (a) $\mathrm{Pe} \sim O(0.01)$, (b) $\mathrm{Pe} \sim O(1)$.

As shown in Fig. 5 (a), for low Pe at low water saturation $S_w = 0.20$, methane hydrate dissociation occurs primarily near the gas phase when the methane concentration in gas decreases by depressurisation. The interface shape remains almost unchanged due to the low flow rate, and the methane molecule in the water phase diffuses through the gas-water interface into the gas. Due to the low diffusivity of methane in water, only near the gas-water interface does C_w decrease appreciably, while other locations away from the interface still maintain high values of C_w. The high concentration limits the methane hydrate dissociation rate in the water phase, regarded as the mass transport limitation, leading to a predominance of dissociation front only in the gas phase and in the vicinity of the gas-water interface. Therefore, the hydrate enclosed in the gas phase is substantially dissolved in the late dissociation stage ($t = 5$ s). In contrast, a significant proportion of hydrates in the water phase are still present

due to the mass transport limitation.

Microfluidic experiments are also conducted to examine the behaviour of methane hydrate dissociation to verify the aforementioned numerical results. The experimental apparatus and procedure are similar to previous work (Almenningen et al., 2017; Wang et al., 2021) and are not detailed here. Initially, methane hydrate is formed at $T = 274.15$ K, $p = 5$ MPa, after which the pressure in the microfluid chip plummets to $p = 1$ MPa, leading to the hydrate dissociation. Fig. 6 presents the experimental image of a specific site before and after 1 second at a certain stage of the dissociation process. The red dashed box in the right panel of Fig. 6 denotes the pre-dissociation hydrate structure in the left panel to highlight the hydrate structure evolution. The hydrate surface is covered by gas and water on two sides, respectively. The fact that the hydrate considerably decomposes on its gas-covered side but not on its water-covered side suggests that the water layer on the hydrate significantly slows down the dissociation process. This phenomenon can be attributed to the mass transport limitation in water, which shows excellent agreement between experimental and numerical observations.

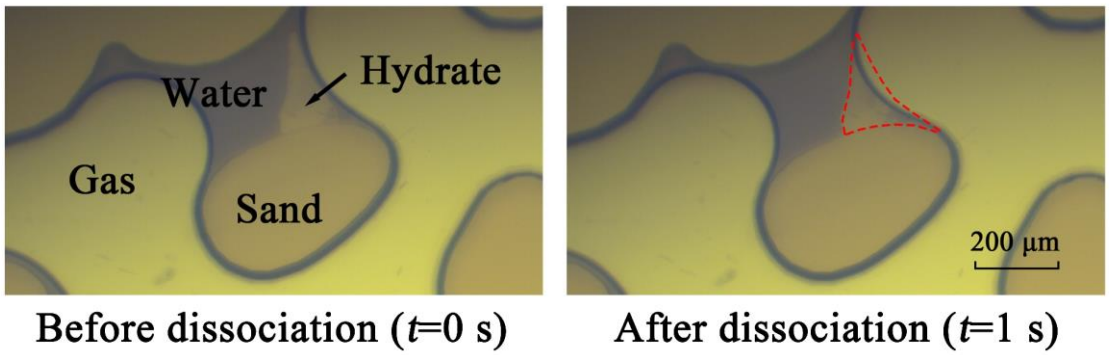

Fig. 6. Microfluidic experimental image of methane hydrate dissociation process by depressurisation.

As illustrated in Fig. 5(b), the multiphase flow exhibits a distinct pattern when Pe is high. Mass transport limitation still plays an important role and the methane concentration in the

water phase away from the interface remains high. The concentration distribution differs significantly from the low Pe condition because of the deformation of the gas-water interface and the increased advection effect. By interfacing with the gas phase, the initial water-encapsulated hydrate has the chance to lower the local methane content and facilitate hydrate dissociation there. The hydrate dissociation rate is extremely slow for low Pe, as seen by the blue circles in Fig. 5, leaving a significant amount of hydrate behind. Interfacial mass movement with an advection effect lowers the concentration at the same site when the fluid velocity is high because the gas phase can pass through there. Therefore, the hydrate in the blue circle of Fig. 5(b) undergoes visible dissociation compared with the low Pe condition.

In Fig. 5, the water saturation is low, thus the gas covers the majority of the hydrate in the sediment and most of the hydrate can be dissolved in both low and high Pe circumstances. Therefore, it is difficult to measure how the interface movement affects the hydrate dissociation rate, as shown in Fig. 4. When the water saturation is high, such as $S_w = 0.50$, the situation is quite different. In Fig. 7, except for the region close to the interface, the concentration is still high across much of the water body, demonstrating that mass transport limitations play a substantial impact. Since hydrate dissociation mostly takes place in the gas phase, Fig. 4 shows a reduced overall hydrate dissociation rate due to the increased water saturation. As seen in Fig. 7(a), the hydrate covered by gas is depleted at t=5 s when Pe is low, exposing the surface of the sand particles. Because the hydrate in the gas phase has already been consumed, methane hydrate dissociation can only now slowly take place in the water phase. As a result, as seen in Fig. 4, the total dissociation rate in the late stage becomes quite constrained. In contrast, with large Pe, as seen in Fig. 7(b), the gas bubbles undergo severe distortion and displacement during

fluid flow. The blue circles represent the areas where some water-covered hydrates have made contact with the gas phase due to the movement of the gas bubbles. As a consequence, the gas-covered hydrate continues to participate in the dissociation even at a later stage, maintaining the dissociation rate. In Fig. 4, the increased fluid velocity at the same high water saturation condition causes a much greater dissociation rate.

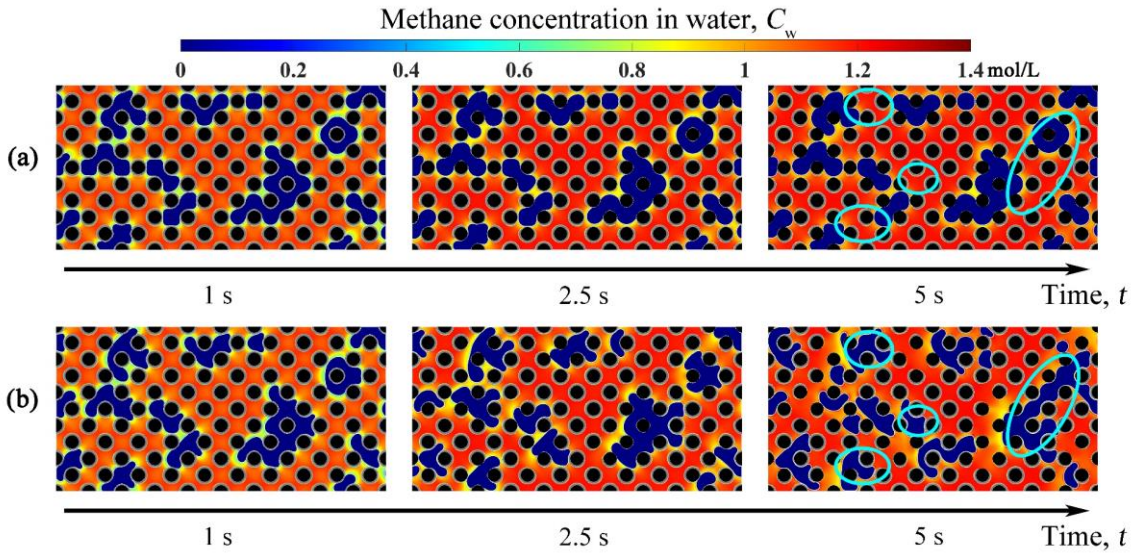

Fig. 7. The temporal evolution of methane concentration in water during methane hydrate dissociation in the GC sediment of $S_{h0} = 0.27$ and $S_w = 0.50$ at (a) $\mathrm{Pe} \sim O(0.01)$, (b) $\mathrm{Pe} \sim O(1)$.

In conclusion, the hydrate dissociation kinetic behaviour is significantly influenced by mass transport limitation. Due to the poor diffusivity, the methane concentration remains high, resulting in the dissociation primarily taking place in the gas phase. Therefore, the dissociation rate becomes slower when water saturation increases. For high Pe, the migration of gas bubbles helps the previously water-covered hydrate to be exposed to the gas phase, which consequently accelerates the hydrate dissociation rate in the region of high water saturation.

3.1.2 Methane hydrate dissociation under non-isothermal conditions

After modelling isothermal methane hydrate dissociation processes to identify the mass transport limitation mechanism, the thermal effect and competition mechanisms between heat and mass transport are investigated by taking the reaction heat into account. In the simulation, various water saturations and fluid flow rates are used, and the resulting hydrate conversion ratio curves are displayed in Fig. 8. The hydrate dissociation rate decreases as water saturation increases, consistent with the results obtained under isothermal conditions. Compared to the isothermal results in Fig. 4, the hydrate dissociation rate decreases significantly when the reaction heat is accounted for with the greatest conversion rate only reaching less than 20%. As opposed to isothermal situations, the difference between low and high Pe under the same water saturation is negligible.

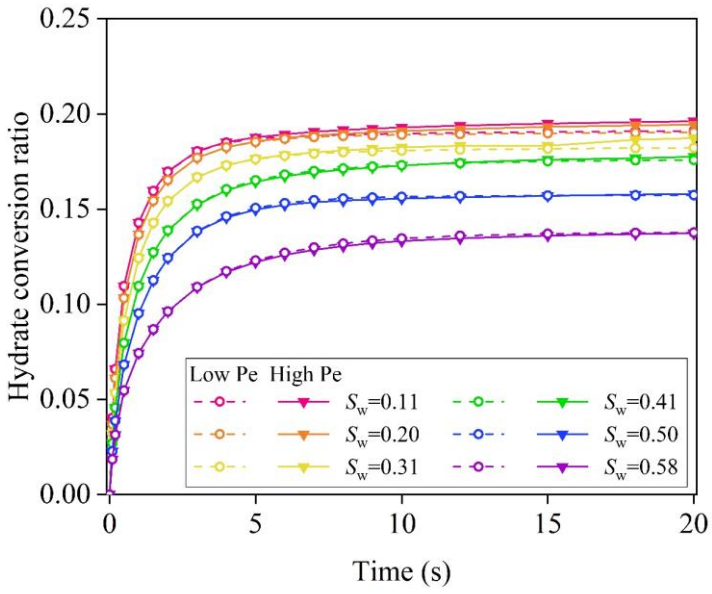

Fig. 8. Comparison of non-isothermal hydrate conversion ratio curves under different S_w and Pe conditions.

To explain the different hydrate conversion with isothermal and non-isothermal conditions, methane concentration and temperature evolution in four representative cases, respectively

$S_w = 0.20$ and $S_w = 0.50$ at high $\mathrm{Pe} \sim O(1)$ and low $\mathrm{Pe} \sim O(0.01)$, are closely analysed to recognize the heat and mass transport characteristics. Fig. 9 shows the temporal evolution of methane concentration in water C_w and temperature T for the low Pe case with the water saturation of $S_w = 0.20$, whereas numerical results of the other three cases are presented in the Supplement Material for brevity (Fig. S3-S5). The evolution of the methane hydrate concentration follows similar patterns to the isothermal conditions in Fig. 5, where the concentration in water distant from the gas-water interface maintains a high level. The methane hydrate dissociation front is highlighted by grey/black lines in the temperature contour of Fig. 9(b), which is derived by calculating the hydrate volume drops before and after the dissociation. As in the isothermal situation, it can be seen that the dissociation front dominates in the gas phase. As a result, the mass transfer limitation mechanism continues to significantly impact the dynamics of hydrate dissociation under non-isothermal conditions. This is the cause of the dissociation rate decreasing with increasing water saturation, as examined in the previous section.

After some hydrate is dissociated, the endothermic dissociation reaction induces a remarkable drop in temperature throughout the sediment shown in Fig. 9 at $t = 5$ s. Eventually, the sediment temperature generally falls to the final equilibrium state of approximately 280 K at $t = 10$ s, with the local temperature difference being unimportant due to adequate conjugate heat transmission. The reduction in the dissociation rate induced by temperature decrease is referred to as heat transport limitation. Therefore, an extremely slow dissociation rate is observed in both the water and gas phase due to the kinetic (Eq. (8)) and thermodynamic (Eq. (10)) reasons. This explains why, when the reaction heat is taken into account, the hydrate

dissociation rate reduces dramatically in Fig. 8 when compared to the isothermal simulations in Fig. 4.

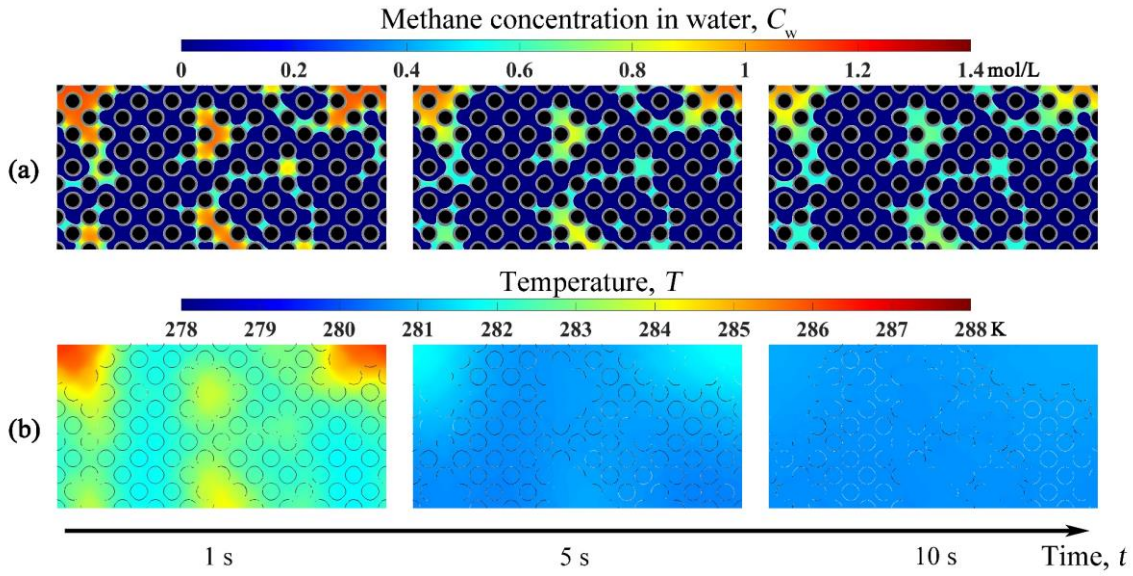

Fig. 9. The temporal evolution of (a) methane concentration in water and (b) temperature during methane hydrate dissociation in the GC sediment with $S_w = 0.20$, $\mathrm{Pe} \sim O(0.01)$ and $S_{h0} = 0.27$. The grey/black lines in the temperature contour denote the dissociation front.

In contrast to the isothermal situation, the hydrate on the sand is never completely depleted because of the low hydrate conversion ratio shown in Fig. 9. Regardless of the multiphase flow pattern, the gas phase is constantly in contact with the hydrate, hence there is no variation in the dissociation rate caused by bubble migration. The conversion curves in Fig. 8 for high and low Pe conditions thus largely overlap.

To obtain a quantitative perspective on the competitive mechanism of heat and mass transport limitation, three typical simulations are conducted at each water saturation: (1) single-phase isothermal dissociation; (2) multiphase isothermal dissociation; (3) multiphase non-isothermal dissociation. The differences among these three situations can characterise the extent of heat and mass transport limitations, which is fully explained in our present work

(Yang et al., 2022b). Fig. 10 shows the difference in the hydrate conversion ratio among the three situations for different water saturations at $t = 1\,\mathrm{s}$, with the amount of heat and mass transport limitations marked. As the water saturation increases, the dissociation dynamics shifts from being dominated by the heat transport limitation to being dominated by the mass transport limitation. The disparity between the conversion curves for different water saturations is decreased as a result of the reduced heat transport limitation partially balancing the increased mass transport limitation. Therefore, both heat and mass transport mechanisms must be completely taken into account when computing the methane hydrate dissociation kinetic model under the non-isothermal condition.

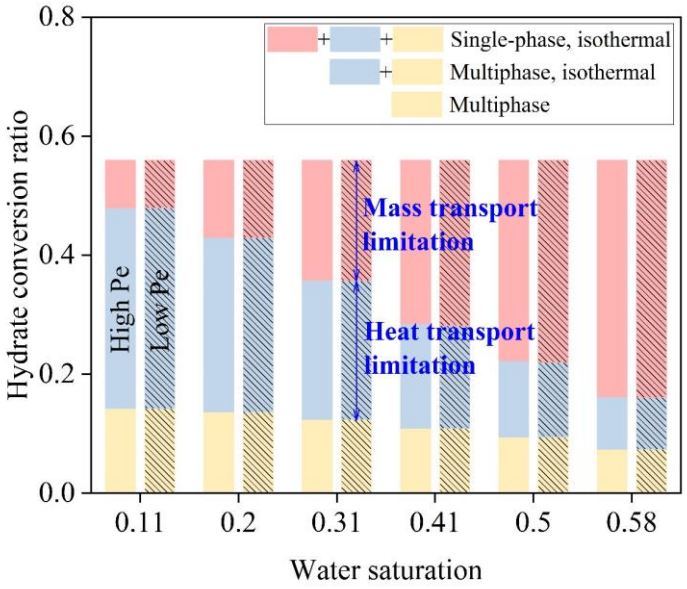

Fig. 10. Quantification of the heat and mass transport limitations under different water saturations and fluid flow rates. The clean bars represent high Pe, and the shaded bars represent low Pe.

3.1.3 Implications for upscaling the kinetic model

Based on the above mechanistic analyses, both heat and mass transport limitations are critical factors determining the dissociation kinetic behaviour. This perception brings enlightening insights into the upscaling of the dissociation kinetic model.

As for the consideration of mass transport limitation, it is known from numerical and experimental results that methane hydrate dissociation mainly occurs on the hydrate surface covered by the gas phase. Therefore, the effective reaction surface area A_{ers}, which is defined as the area of the exposed hydrate surface to the gas phase, dominates the dissociation front. Fig. 11 illustrates the variation of effective reaction surface area A_{ers} against the hydrate saturation during the isothermal dissociation dynamics. A_{ers} drops as water saturation rises, which causes the dissociation rate to fall as well, which is consistent with the behaviour in Fig. 4 and Fig. 8.

For low Pe shown in Fig. 11(a), all the A_{ers} scatter plots exhibit a typical three-stage structure regardless of the water saturation. The example of $S_w = 0.31$ is used to demonstrate the physical implication of the three-stage structure. In the first stage, the effective reaction surface area A_{ers} stays plateaued because the hydrate remains to cover the sand surface despite some hydrate being dissolved. Considering the effective reaction surface area of the first stage as a constant A_{ers0}, this constant value decreases with increasing water saturation S_w. As the hydrate structure is further dissolved in the second stage beginning at point *a*, some of the sand particle surface starts to get exposed, triggering a rapid parabolic decrease in A_{ers}. A_{ers} decreases to zero and the third stage begins, when all of the hydrate accessible to the gas phase is consumed at point *b*.

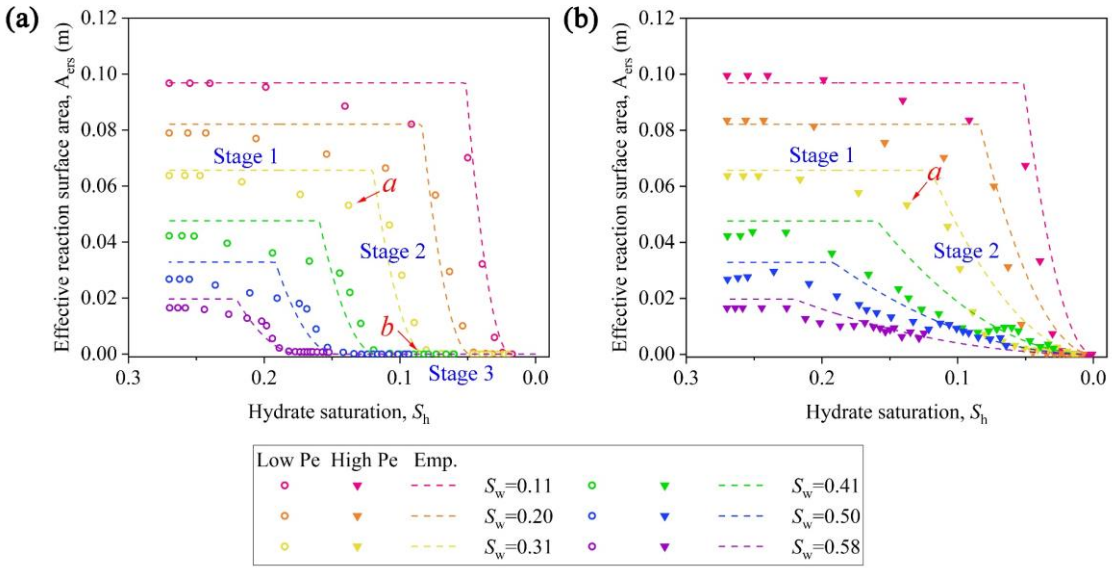

Fig. 11. Evolution of effective reaction surface area A_{ers} against the hydrate saturation during dissociation process at (a) low Pe, (b) high Pe in the sediment of GC, $S_{h0} = 0.27$. The dash lines denote the fitting curves of A_{ers} computed by Eq. (34).

For high Pe shown in Fig. 11(b), the effective reaction surface area presents a distinct pattern, a two-stage scheme. Despite the rapid fluid flow rate, A_{ers} still maintains a constant in the first stage, which is similar to the low Pe condition. As the dissociation advances and some hydrate on the sand surface are depleted, A_{ers} begins to decline rapidly at point a and the second stage starts. Due to the deformation and movement of the gas bubble at high flow rates, A_{ers} does not decrease to zero, hence the third stage does not occur in contrast to low Pe. The first-stage effective reaction surface area constant A_{ers0} and start points of the second stage a are generally consistent with low Pe at the same water saturation. However, because there is no third stage under the high Pe condition, A_{ers} is greater than the low Pe in the last dissociation moment. This explains why the methane hydrate dissociation rate is more rapid for high Pe in Fig. 4. Since the hydrate conversion ratios are all less than 20% for the non-isothermal condition, the effective reaction surface area variation essentially remains in the

first stage for both high and low Pe situations. Therefore, the conversion curves for different fluid flow rates appear to have little variation in Fig. 8. In summary, the effective reaction surface area variation can effectively explain the dissociation kinetic behaviour induced by mass transport limitation. According to pore-scale physics, the effect of mass transport limitation on the dissociation rate can be quantified by directly replacing $F_A A_s$ in Eq. (29) by the effective reaction surface area A_{ers}.

The effect of temperature decreases on the dissociation rate should be accounted for when considering the heat transport limitation. As stated above, the local temperature difference is not significant within the pore structure during dissociation, which is consistent with the conclusion in our previous work (Yang et al., 2021b; Yang et al., 2022b). The local thermal equilibrium assumption is valid for the hydrate dissociation process. Therefore, the classical one-temperature model Eq. (28) is reasonable to compute the volume-average energy equation at the REV scale without significant loss of accuracy compared to the thermal non-equilibrium model (Liao et al., 2022). Since the heat transport limitation can be characterised by the volume-averaged temperature via the term $\exp\left(E_A / R\overline{T}\right)$ in Eq. (29), the effect of heat transfer may not need to be accounted for in the pre-exponential factor $\tilde{k}_0$. Considering the mass transfer limitation has been considered by $F_A A_s$, the intrinsic kinetic parameter k_0 in Eq. (8) can be directly adopted as $\tilde{k}_0$ in Eq. (29). Eventually, the hydrate dissociation kinetic model can be scaled up based on the above mechanistic insights. The upscaled kinetic model will be verified by comparing the pore-scale and the REV-scale results in Section 3.2.2.

3.2 Upscaling methane hydrate kinetic model from pore scale to REV scale

3.2.1 Effective reaction surface area model

A reliable effective reaction surface area model is required to quantify the mass transport limitation effect in the upscaling procedure. According to the three-stage evolution of A_{ers} for low Pe depicted in Fig. 11(a), the effective reaction surface area model can be broken down into three parts. In the first stage, the plateaued A_{ers} can be defined as a constant A_{ers0}, which reduces with increasing water saturation. Thus, the effective reaction area A_{ers0} should be proportional to the ratio of gas phase and fluid phase as

$$A_{ers0} = A_{s0} \frac{S_g}{S_g + S_w} = A_{s0} \left(1 - \frac{S_w}{1 - S_h} \right) \tag{31}$$

where $A_{s0} = 0.12$ m is the total hydrate surface area at initial, which is computed directly based on the morphology in Fig. 1. To verify this relationship, A_{ers0} for different water saturations are plotted and linearly fitted in Fig. 12. The fitting result is

$$A_{ers0} = A_{s0} \left(0.95 - 1.43 \cdot S_w \right) \tag{32}$$

with $R^2 = 0.9962$. The fitting result has a similar form as Eq. (31), demonstrating the relationship in Eq. (31) can be used to estimate the effective reaction surface area in the first stage.

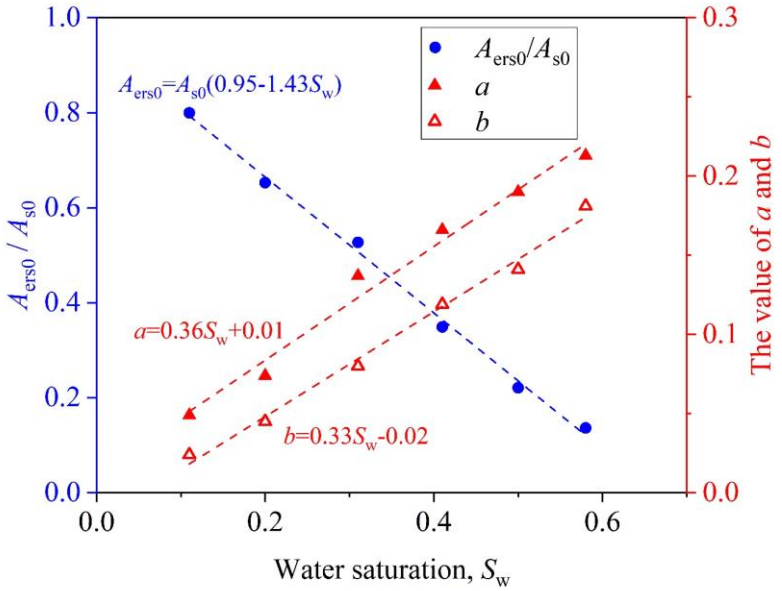

Fig. 12. The value of A_{ers0} (left, blue), a and b (right, red) against the water saturation in the GC sediment with $S_{h0} = 0.27$. The dash lines are fitting results.

In the second stage, the effective reaction surface area shows a rapid parabolic decline. The start and end points for the second stage, a and b, exhibit a significant linear correlation to the water saturation S_w, as shown in Fig. 12, which can be fitted as

$$\begin{aligned} a &= 0.36S_w + 0.01 \\ b &= 0.33S_w - 0.02 \end{aligned} \tag{33}$$

with $R^2 = 0.9815$ and $R^2 = 0.9912$ respectively. Then, A_{ers} drops to zero, entering the third stage. Based on the analyses for low Pe, the mass transport limitation can be quantified by the effective reaction surface area A_{ers} to replace $F_A A_s$ in Eq. (29) as the following empirical formula

$$F_A A_s = A_{ers}\left(S_h, S_w\right) = \begin{cases} A_{s0}\left(1-\dfrac{S_w}{1-S_h}\right) & S_h > a \\ A_{s0}\left(1-\dfrac{S_w}{1-S_h}\right)\left(\dfrac{S_h-b}{a-b}\right)^2 & b \le S_h \le a \\ 0 & S_h < b \end{cases} \quad (34)$$

where a and b can be defined by Eq. (33) in the GC sediment with $S_{h0} = 0.27$. The value of a and b should be restricted to the interval $[0, S_{h0}]$ once the value calculated by Eq. (33) is out of this range. The dashed line in Fig. 11(a) denotes the A_{ers} curves calculated from the empirical model Eq. (34), which show acceptable agreement with the numerical results.

When Pe is high, the effective reaction surface area also experienced a first plateau and a second parabolic decline stage similar to the low Pe condition. Therefore, A_{ers} can also be computed by Eq. (34) but b is set as zero due to the absence of the third stage. The empirically calculated curves of A_{ers} are shown in Fig. 11(b), also demonstrating high predictability. It should be noted that when the hydrate structure is different such as the pore-filling structure, the model parameters of A_{ers} should be adapted accordingly, which will be discussed in the later section.

3.2.2 Validation of upscaled kinetic model

From the above discussion, heat and mass transport limitations are the primary mechanisms affecting the dissociation rate, which is related to temperature and concentration evolution due to the dissociation reaction as well as the gas-water distribution and migration. These two mechanisms should be quantified at the REV scale to upscale the kinetic model for methane hydrate dissociation. It is already recognised that the effective reaction surface area can quantify the mass transport limitation and that a one-temperature model based on the local

thermal equilibrium assumption can compute the heat transport limitation. Based on the REV-scale governing equations (26)-(29) without consideration of the flux term, combining with the pore-scale understanding of the heat and mass transport mechanisms, the kinetic model within a single REV can be derived by the following set of equations

$$F_A A_s = A_{ers} = f\left(S_h, S_w\right) \tag{35}$$

$$\dot{r} = -k_g \exp\left(\frac{E_A}{R\bar{T}}\right) F_A A_s \left(C_{eq,g} - \bar{C}_g\right) \tag{36}$$

$$\frac{d\bar{C}_g}{dt} = \frac{-\dot{r}}{S_g V \phi_{por}} \tag{37}$$

$$\frac{d\bar{T}}{dt} = \frac{\dot{r} \cdot \Delta H}{\sum_{i=g,w,h} S_i \rho_i c_{pi} V \phi_{por} + \rho_s c_{ps} V \left(1-\phi_{por}\right)} \tag{38}$$

$$\frac{dS_h}{dt} = \frac{\dot{r} V_M}{V \phi_{por}}, \ \frac{dS_w}{dt} = \frac{\dot{r} n_H M W_w}{\rho_w V \phi_{por}}, \ S_g = 1 - S_h - S_w \tag{39}$$

where the dissociation rate $\dot{r}$ is determined by the volume-averaged concentration in the gas phase $\bar{C}_g$ and the volume-averaged temperature $\bar{T}$. V denotes the REV volume and MW is the molar mass. The governing equations (35)-(39), which have the form of an ordinary differential equation (ODE), are built for a zero-dimensional REV that ignores advection and diffusion transfer between the neighbouring REVs. The ODE model is perfectly appropriate for analyses since the present work concerns the kinetic model inside a single REV with periodic boundaries in the pore-scale numerical simulation. The ODE model can be easily extended to the partial differential equations by involving the spatial heat and mass flux between REVs, commonly found in most REV-scale solvers (Yin et al., 2016). Eq. (35) and (37) characterise the effect of mass transport limitation by simulating the effective reaction surface area variation during the hydrate dissociation. The decrease of dissociation rate due to

the mass transport limitation is believed to be fully reflected directly by A_{ers} without adjustment of the intrinsic kinetics k_g as discussed in Section 3.1. Eq. (38) account for the heat transport limitation based on the one-temperature model assumption. The fourth-order Runge-Kutta method is used to solve the ODE model.

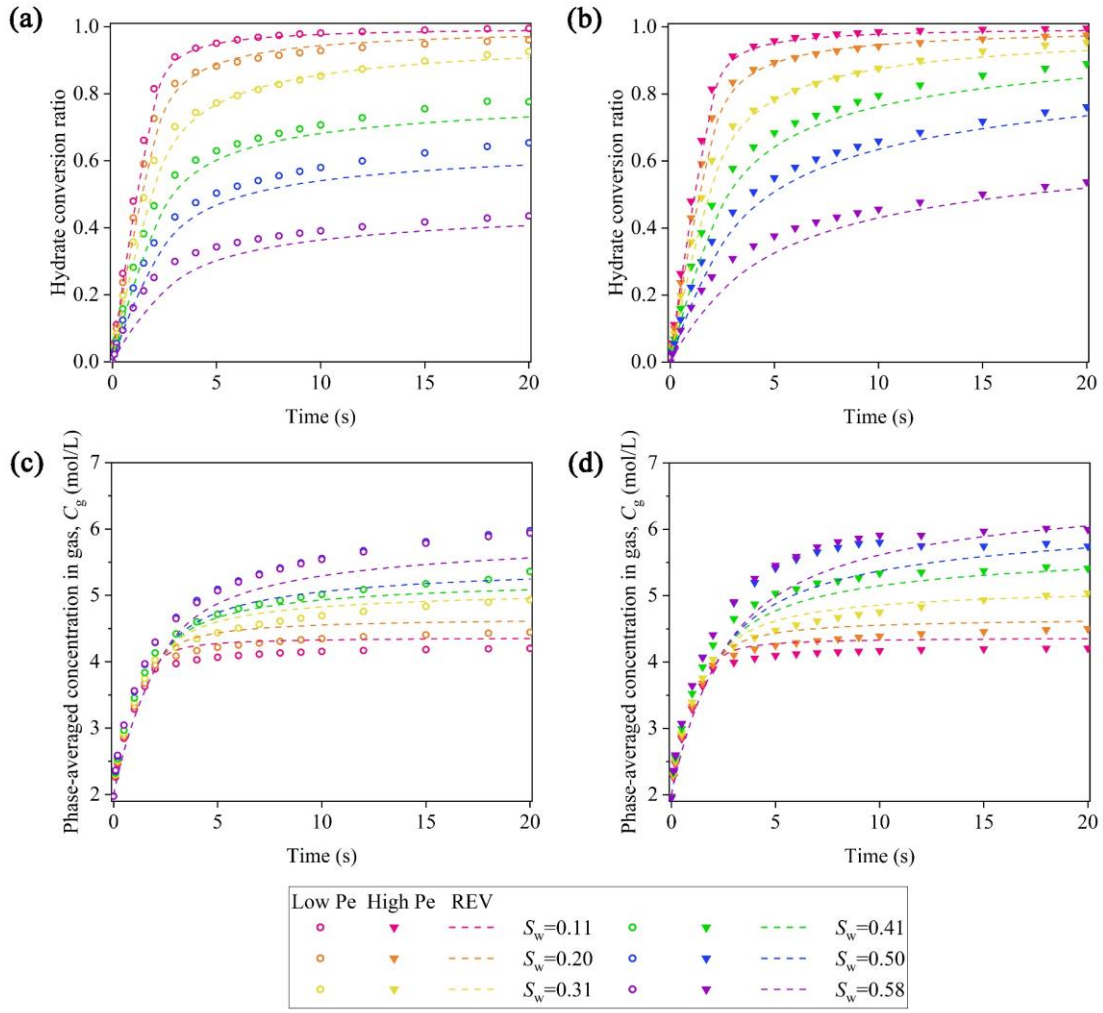

Fig. 13. Comparison of REV-scale results predicted by the upscaled kinetic model (dash line) and pore-scale numerical results (scatter) of (a) hydrate conversion ratio for low Pe; (b) hydrate conversion ratio for high Pe; (c) phase-average methane concentration in gas for low Pe; (d) phase-average methane concentration in gas for high Pe during the isothermal dissociation process.

The isothermal dissociation dynamics in the GC sediment with $S_{h0} = 0.27$ are first

investigated for validation. Fig. 13 shows the upscaling result plotted by the dashed line agrees well with the pore-scale numerical results for both low and high Pe, with relative errors ranging from 2% to 5% for various water saturations. Meanwhile, the temporal evolution of the phase-averaged concentration in the gas phase is also well predicted. These excellent consistencies suggest that the upscaling kinetic model successfully accounts for the mass transport limitation mechanism, involving the effect of water saturation and fluid flow rate on the hydrate dissociation.

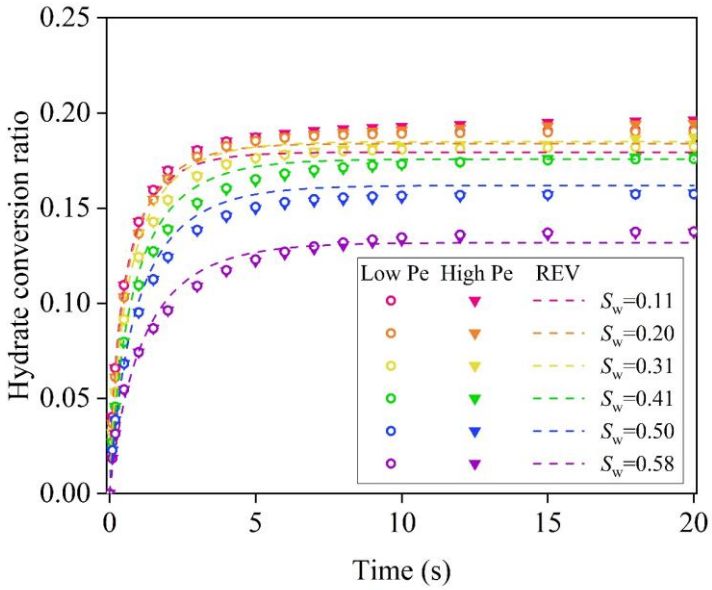

Fig. 14. Comparison of REV-scale results predicted by the upscaled kinetic model (dash line) and pore-scale numerical results (scatter) of hydrate conversion ratio during the non-isothermal dissociation process.

Afterward, the non-isothermal dissociation dynamics considering both heat and mass transport limitations is predicted with the upscaling kinetic model, which is then compared with the pore-scale numerical results in Fig. 14 and 15. Fig. 14 indicates that the upscaling kinetic model accurately predicts the dissociation rate under various conditions of water

saturation and Pe. The relative deviations of the hydrate conversion ratio between the prediction and simulation results are less than 6% for all cases. The predicted phase-averaged concentration and volume-averaged temperature are also accurately calculated, as illustrated in Fig. 15, demonstrating that the upscaling kinetic model effectively captures the heat and mass transport mechanisms under the non-isothermal condition. Therefore, compared to the conventional production forecast solvers based on history matching (Yin et al., 2018), the present model is developed from pore-scale physics and can adapt to the various range of reservoir conditions (S_w) and production scenarios (Pe).

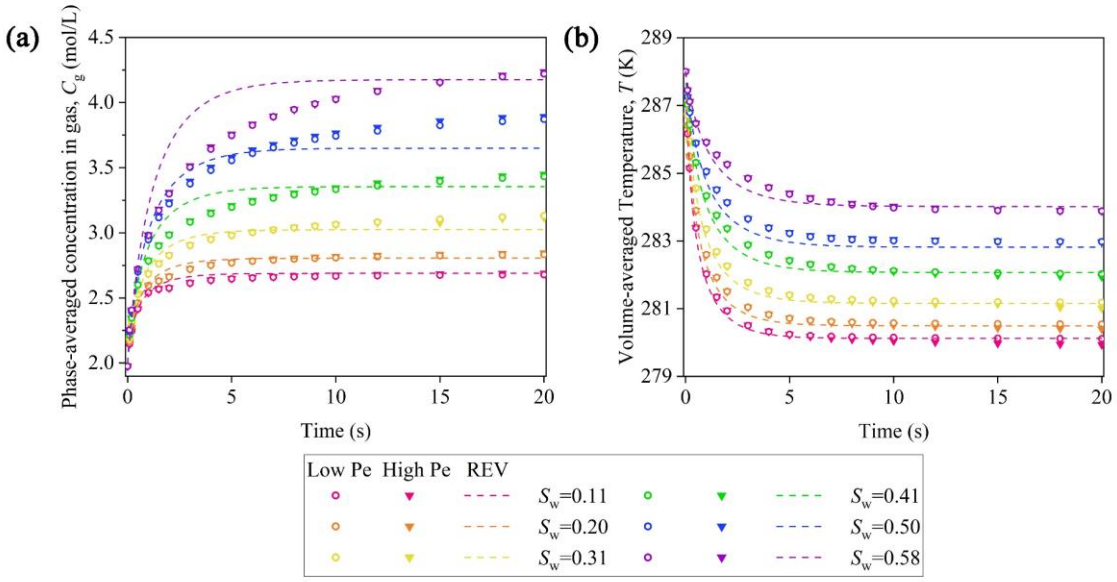

Fig. 15. Comparison of REV-scale results predicted by the upscaled kinetic model (dash line) and pore-scale numerical results (scatter) of (a) phase-averaged methane concentration in the gas phase, (b) volume-averaged temperature during the non-isothermal dissociation process.

3.3 Effect of methane hydrate pore habits on upscaling kinetic models

The hydrate pore habit influences the transport properties of the sediment, and hence the dissociation dynamics. Therefore, the hydrate dissociation kinetic model should be impacted

by the hydrate pore habits. In this section, various hydrate pore habits shown in Fig. 1 are applied to investigate their effect on the dissociation kinetics. A moderate water saturation $S_w = 0.41$ is used in the simulation. Fig. 16 shows the concentration and temperature variations at low Pe in a typical pore-filling (PF) sediment with $S_{h0} = 0.27$. For high Pe, the numerical results are shown in Figure S6. Regarding the preferential hydrate dissociation close to the gas phase and the considerable temperature drop with the local temperature difference, the heat and mass transport mechanisms are comparable to the grain-coating cases in Fig. 9. The difference is the hydrate pore habit changes the multiphase flow dynamics and the dissociation front morphology, eventually shifting the effective reaction surface area A_{ers}. Therefore, the upscaling kinetic model should correct the variation of A_{ers} with the hydrate pore habits.

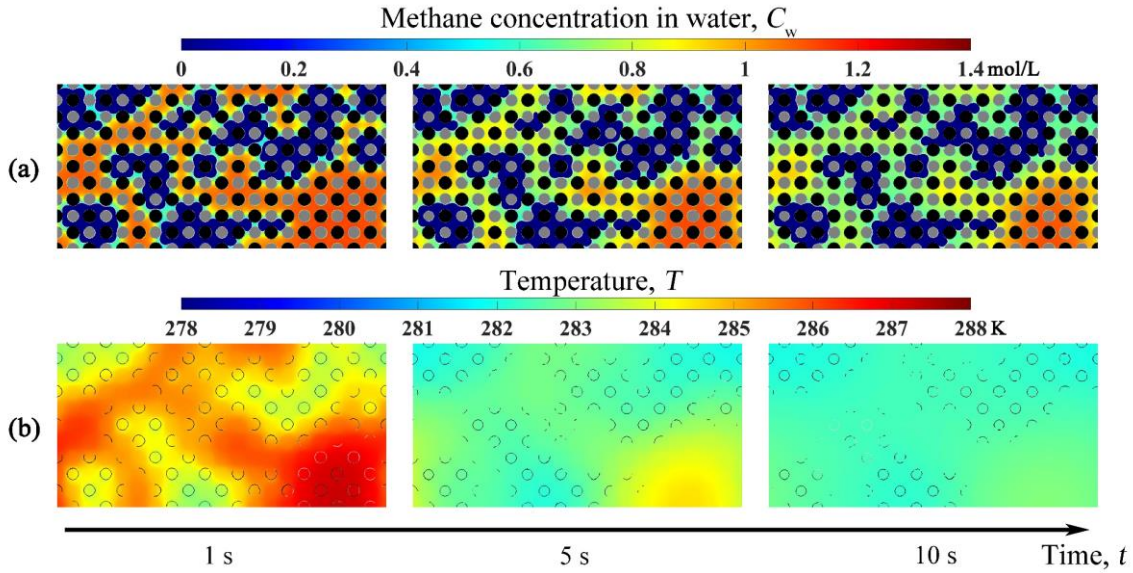

Fig. 16. The temporal evolution of methane concentration in water and temperature during methane hydrate dissociation in the PF sediment with $S_w = 0.41$, $\mathrm{Pe} \sim O(0.01)$ and $S_{h0} = 0.27$.

The isothermal dissociation dynamics under different hydrate pore habits is investigated

to highlight the evolution of A_{ers}. Fig. 17 compares the hydrate dissociation rates between different sediment structures at low and high Pe conditions with the water saturation of $S_w = 0.41$. The dissociation rate increases as the hydrate saturation rise. For the same hydrate saturation, the dissociation rate in the grain-coating sediment is slightly higher than pore-filling, and it is approximately the same in heterogeneous and homogeneous structures.

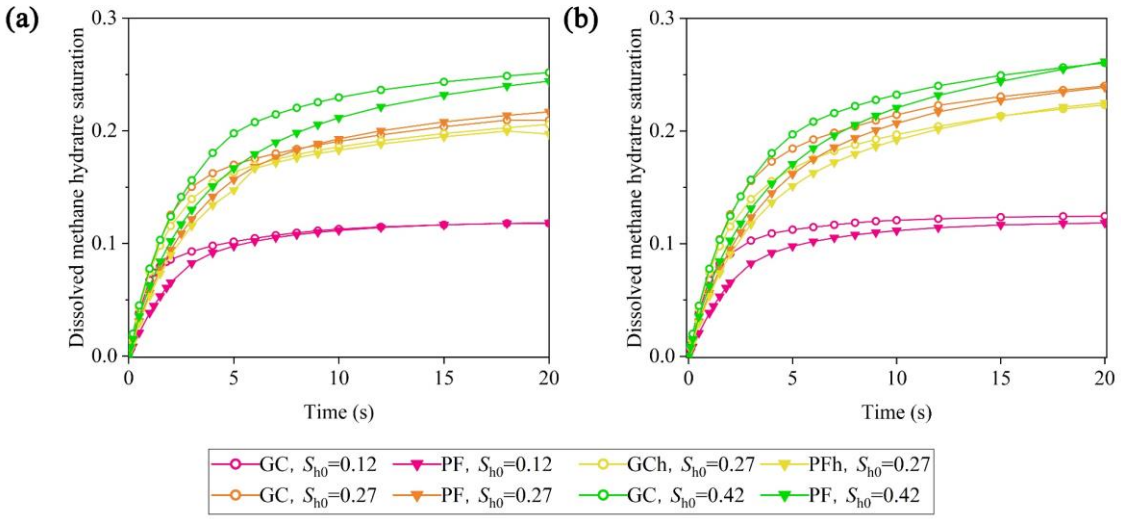

Fig. 17. Comparison of methane hydrate dissociation rates for different methane hydrate pore habits at (a) low Pe, (b) high Pe during isothermal dissociation.

The variation of A_{ers} under different sediment structures is calculated in Fig. 18 to understand the comparison results above. As seen, the effective reaction surface area A_{ers} increases with hydrate saturation for both grain-coating and pore-filling structures. When given the same hydrate saturation, A_{ers} are more extensive in the grain-coating sediment than in the pore-filling sediment since the A_{s0} for the pore-filling habit ($A_{s0} = 0.09$ m for PF, $S_{h0} = 0.27$) is less than the grain-coating habit ($A_{s0} = 0.12$ m for GC, $S_{h0} = 0.27$) . The A_{ers} appears to be consistent for heterogeneous and homogeneous structures. These patterns of effective reaction surface area are the underlying factors for the above dissociation rate characteristics.

It can be observed that for all the grain-coating structures, the evolution of A_{ers} has similar schemes as that of section 3.2.1, including the first stage of plateauing, the second stage of parabolic decline and the third stage of dropping completely to zero (only for low Pe), which can be described mathematically by Eq. (34). Notably, Fig. 18 indicates that the A_{ers} of the pore-filling sediment also displays the typical three-stage characteristics. After a short plateau in the first stage, the effective reaction surface area almost linearly decreases in the second stage, as opposed to the parabolic decline in the grain-coating sediment. This is because the hydrate surface gradually decreases with the shrinking of the dispersed hydrate grains in the pore-filling sediment. In contrast, the hydrate surface changes little with dissociation, but it abruptly drops to zero when the hydrate covering the sand is exhausted in the grain-coating sediment. In the third stage for low Pe, the hydrate accessible to the gas phase is consumed and the A_{ers} drops to zero. For high Pe, the rapid gas bubble migration results in the hydrate always being in contact with the gas phase, and thus there is no third stage.

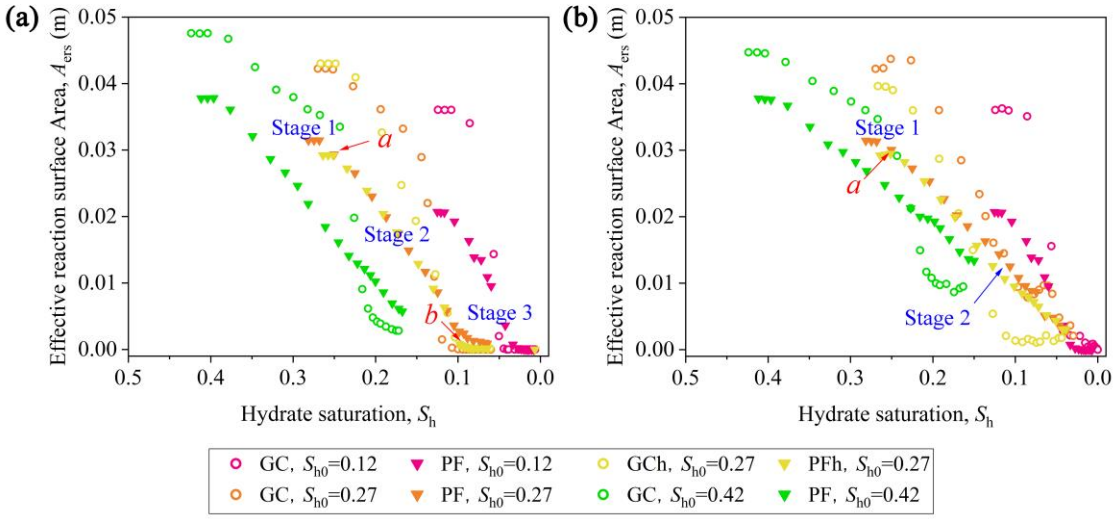

Fig. 18. Comparison of effective reaction surface area for different methane hydrate pore habits at (a) low Pe, (b) high Pe during isothermal dissociation.

Based on the above analysis, for the pore-filling structures, the effective reaction surface

area can be calculated to replace $F_A A_s$ in Eq. (29) by the following equation similar to Eq. (34) as

$$F_A A_s = A_{ers}\left(S_h, S_w\right) = \begin{cases} A_{s0}\left(1-\dfrac{S_w}{1-S_h}\right) & S_h > a \\ A_{s0}\left(1-\dfrac{S_w}{1-S_h}\right)\left(\dfrac{S_h-b}{a-b}\right) & b \le S_h \le a \\ 0 & S_h < b \end{cases} \tag{40}$$

where b should be zero for the high Pe situation. The values of a and b for both grain-coating and pore-filling structures need to be adjusted accordingly for different S_{h0}, which can be obtained by fitting the numerical results as section 3.2.1, and will not be discussed in depth here.

4. Conclusions

In the present work, pore-scale numerical simulations of methane hydrate dissociation by depressurisation are conducted to understand the effects of multiphase heat and mass transport limitation mechanisms on dissociation kinetic behaviour. Based on the mechanical knowledge, the methane hydrate dissociation kinetic model is then upscaled for REV-scale modelling and carefully verified by the pore-scale numerical simulations.

During methane hydrate dissociation by depressurisation, methane concentration in the water phase maintains a high value due to the low diffusivity, leading to the dissociation mainly occurring in the gas phase as the mass transport limitation. Due to the heat absorption of the endothermic dissociation reaction, temperature decreases significantly, resulting in the limited dissociation rate from the kinetic and thermodynamic aspects as heat transport limitation. The local temperature difference is not significant through the sediment, indicating the local thermal

equilibrium. Heat and mass transport limitations are both critical factors determining dissociation kinetic behaviour.

Based on the mechanistic knowledge, the methane hydrate dissociation kinetic model for the REV scale is constructed. Combining the continuum theory, the kinetic model considering heat and mass transport limitation mechanisms is proposed based on Eqs. (26)-(29). The effective reaction surface area A_{ers} is proposed to replace $F_A A_{\mathrm{s}}$ in Eq. (29) for quantifying the mass transport limitation effect, and the formulation to calculate A_{ers} is provided as Eqs. (34) and (40). Based on the local thermal equilibrium assumption, the temperature decrease due to the endothermic reaction can be obtained using the one-temperature model. The predictions by the upscaled kinetic model and numerical simulation results are in good agreement, demonstrating the proposed kinetic model is reliable. The controlling mechanisms of dissociation kinetics are similar in different methane hydrate pore habits and the different dissociation rates between hydrate structures can be represented by the change of effective reaction surface area.

The present work proposes the kinetic model for REV-scale modelling by fully involving the mechanisms of heat and mass transport limitation, which is applicable for diverse sediment (S_{w}, S_{h}) and production (Pe) conditions. It is expected to guide the programme design and production forecast for methane hydrate extraction. The present work is an attempt to upscale the kinetic model, which still has some limitations due to the two-dimensional idealized structure used. In the future, pore-scale modelling will be conducted within realistic three-dimensional digital rock structures to obtain a more reasonable A_{ers} model for upscaling.

Acknowledgement

This work was financially supported by the National Natural Science Foundation of China (No. 52206014). Additional support fromthe UK Engineering and Physical Sciences Research Council (EPSRC) under the grant Nos. EP/W026260/1 and EP/R029598/1.

References

Almenningen, S., Flatlandsmo, J., Kovscek, A.R., Ersland, G., Ferno, M.A., 2017. Determination of pore-scale hydrate phase equilibria in sediments using lab-on-a-chip technology. Lab Chip 17, 4070-4076.

Almenningen, S., Iden, E., Fernø, M.A., Ersland, G., 2018. Salinity Effects on Pore-Scale Methane Gas Hydrate Dissociation. Journal of Geophysical Research: Solid Earth 123, 5599-5608.

Anderson, B.J., Kurihara, M., White, M.D., Moridis, G.J., Wilson, S.J., Pooladi-Darvish, M., Gaddipati, M., Masuda, Y., Collett, T.S., Hunter, R.B., Narita, H., Rose, K., Boswell, R., 2011. Regional long-term production modeling from a single well test, Mount Elbert Gas Hydrate Stratigraphic Test Well, Alaska North Slope. Marine and Petroleum Geology 28, 493-501.

Chen, L., Feng, Y., Kogawa, T., Okajima, J., Komiya, A., Maruyama, S., 2018a. Construction and simulation of reservoir scale layered model for production and utilization of methane hydrate: The case of Nankai Trough Japan. Energy 143, 128-140.

Chen, X., Verma, R., Espinoza, D.N., Prodanović, M., 2018b. Pore-Scale Determination of Gas Relative Permeability in Hydrate-Bearing Sediments Using X-Ray Computed Micro-Tomography and Lattice Boltzmann Method. Water Resources Research 54, 600-608.

Chong, Z.R., Yang, S.H.B., Babu, P., Linga, P., Li, X.S., 2016. Review of natural gas hydrates as an energy resource: Prospects and challenges. Applied Energy 162, 1633-1652.

Cui, Y., Lu, C., Wu, M., Peng, Y., Yao, Y., Luo, W., 2018. Review of exploration and production technology of natural gas hydrate. Advances in Geo-Energy Research 2, 53-62.

Dong, F., Zang, X., Li, D., Fan, S., Liang, D.J.E., fuels, 2009. Experimental investigation on propane hydrate dissociation by high concentration methanol and ethylene glycol solution injection. Energy & Fuels 23, 1563-1567.

Feng, Y., Chen, L., Suzuki, A., Kogawa, T., Okajima, J., Komiya, A., Maruyama, S., 2019. Numerical analysis of gas production from layered methane hydrate reservoirs by depressurization. Energy 166, 1106-1119.

Fukumoto, A., Kamada, K., Sato, T., Oyama, H., Torii, H., Kiyono, F., Nagao, J., Temma, N., Narita, H., 2018. Numerical simulation of pore-scale formation of methane hydrate in the sand sediment using the phase-field model. Journal of Natural Gas Science and Engineering 50, 269-281.

Guo, G., Zhang, P., Lei, L., Galindo-Torres, S.A., 2022. A pseudopotential lattice Boltzmann model for simulating mass transfer around a rising bubble under real buoyancy effect. Physics of Fluids 34.

He, Y.L., Liu, Q., Li, Q., Tao, W.Q., 2019. Lattice Boltzmann methods for single-phase and solid-liquid phase-change heat transfer in porous media: A review. International Journal of Heat and Mass Transfer 129, 160-197.

Jamaluddin, A.K.M., Kalogerakis, N., Bishnoi, P.R., 1989. Modelling of decomposition of a synthetic core of methane gas hydrate by coupling intrinsic kinetics with heat transfer rates. The Canadian Journal of Chemical Engineering 67, 948-954.

Ji, C., Ahmadi, G., Smith, D.H., 2001. Natural gas production from hydrate decomposition by depressurization. Chemical Engineering Science 56, 5801-5814.

Kamath, V.A., 1984. Study of heat transfer characteristics during dissociation of gas hydrates

in porous media. Pittsburgh University, PA (USA).

Kang, Q., Lichtner, P.C., Zhang, D., 2006. Lattice Boltzmann pore-scale model for multicomponent reactive transport in porous media. Journal of Geophysical Research: Solid Earth 111, B05203.

Karani, H., Huber, C., 2015. Lattice Boltzmann formulation for conjugate heat transfer in heterogeneous media. Physical Review E 91, 023304.

Kim, H., Bishnoi, P.R., Heidemann, R.A., Rizvi, S.S., 1987. Kinetics of methane hydrate decomposition. Chemical Engineering Science 42, 1645-1653.

Krüger, T., Kusumaatmaja, H., Kuzmin, A., Shardt, O., Silva, G., Viggen, E.M., 2017. The lattice Boltzmann method.

Liao, Y., Zheng, J., Wang, Z., Sun, B., Sun, X., Linga, P., 2022. Modeling and characterizing the thermal and kinetic behavior of methane hydrate dissociation in sandy porous media. Applied Energy 312, 118804.

Maes, J., Soulaine, C., 2018. A new compressive scheme to simulate species transfer across fluid interfaces using the Volume-Of-Fluid method. Chemical Engineering Science 190, 405-418.

Moridis, G.J., 2012. TOUGH+ HYDRATE v1. 2 User's manual: a code for the simulation of system behavior in hydrate-bearing geologic media.

Niu, M., Wu, G., Yin, Z., Sun, Y., Liu, K., Chen, D., 2021. Effectiveness of CO2-N2 injection for synergistic CH4 recovery and CO2 sequestration at marine gas hydrates condition. Chemical Engineering Journal 420, 129615.

Pang, W.X., Xu, W.Y., Sun, C.Y., Zhang, C.L., Chen, G.J., 2009. Methane hydrate dissociation

experiment in a middle-sized quiescent reactor using thermal method. Fuel 88, 497-503.

Ren, X., Guo, Z., Ning, F., Ma, S., 2020. Permeability of hydrate-bearing sediments. Earth-Science Reviews 202, 103100.

Sloan, E.D., 2003. Fundamental principles and applications of natural gas hydrates. Nature 426, 353-359.

Song, R., Sun, S., Liu, J., Yang, C., 2021. Pore scale modeling on dissociation and transportation of methane hydrate in porous sediments. Energy 237, 121630.

Song, Y., Kuang, Y., Fan, Z., Zhao, Y., Zhao, J., 2018. Influence of core scale permeability on gas production from methane hydrate by thermal stimulation. International Journal of Heat and Mass Transfer 121, 207-214.

Song, Y., Yang, L., Zhao, J., Liu, W., Yang, M., Li, Y., Liu, Y., Li, Q., 2014. The status of natural gas hydrate research in China: A review. Renewable and Sustainable Energy Reviews 31, 778-791.

Wang, B., Dong, H., Liu, Y., Lv, X., Liu, Y., Zhao, J., Song, Y., 2018a. Evaluation of thermal stimulation on gas production from depressurized methane hydrate deposits☆. Applied Energy 227, 710-718.

Wang, B., Fan, Z., Zhao, J., Lv, X., Pang, W., Li, Q., 2018b. Influence of intrinsic permeability of reservoir rocks on gas recovery from hydrate deposits via a combined depressurization and thermal stimulation approach. Applied Energy 229, 858-871.

Wang, S., Cheng, Z., Liu, Q., Lv, P., Lv, J., Jiang, L., Song, Y., 2021. Microscope insights into gas hydrate formation and dissociation in sediments by using microfluidics. Chemical Engineering Journal 425, 130633.

Wang, X., Dong, B., Chen, C., Li, W., Song, Y., 2019. Pore-scale investigation on the influences of mass-transfer-limitation on methane hydrate dissociation using depressurization. International Journal of Heat and Mass Transfer 144, 118656.

Wang, X., Dong, B., Li, W., Yu, M., Song, Y., 2018c. Microscale effects on methane hydrate dissociation at low temperature in the micro porous media channels by depressurization. International Journal of Heat and Mass Transfer 122, 1182-1197.

Wang, Y., Li, X.-S., Li, G., Zhang, Y., Li, B., Feng, J.-C., 2013. A three-dimensional study on methane hydrate decomposition with different methods using five-spot well. Applied Energy 112, 83-92.

Yang, J., Dai, X., Xu, Q., Liu, Z., Shi, L., 2022a. Comparative investigation of a lattice Boltzmann boundary treatment of multiphase mass transport with heterogeneous chemical reactions. Physical Review E 105, 055302.

Yang, J., Dai, X., Xu, Q., Liu, Z., Shi, L., Long, W., 2021a. Lattice Boltzmann modeling of interfacial mass transfer in a multiphase system. Physical Review E 104, 015307.

Yang, J., Dai, X., Xu, Q., Liu, Z., Zan, C., Long, W., Shi, L., 2021b. Pore-scale study of multicomponent multiphase heat and mass transfer mechanism during methane hydrate dissociation process. Chemical Engineering Journal 423, 130206.

Yang, J., Xu, Q., Liu, Z., Shi, L., 2022b. Pore-scale study of the multiphase methane hydrate dissociation dynamics and mechanisms in the sediment. Chemical Engineering Journal 430, 132786.

Yang, L., Falenty, A., Chaouachi, M., Haberthür, D., Kuhs, W.F., 2016. Synchrotron X-ray computed microtomography study on gas hydrate decomposition in a sedimentary matrix.

Geochemistry, Geophysics, Geosystems 17, 3717-3732.

Yang, M., Fu, Z., Jiang, L., Song, Y., 2017. Gas recovery from depressurized methane hydrate deposits with different water saturations. Applied Energy 187, 180-188.

Yin, Z., Chong, Z.R., Tan, H.K., Linga, P., 2016. Review of gas hydrate dissociation kinetic models for energy recovery. Journal of Natural Gas Science and Engineering 35, 1362-1387.

Yin, Z., Moridis, G., Chong, Z.R., Tan, H.K., Linga, P., 2018. Numerical analysis of experimental studies of methane hydrate dissociation induced by depressurization in a sandy porous medium. Applied Energy 230, 444-459.

Youslf, M.H., Abass, H.H., Selim, M.S., Sloan, E.D., 1991. Experimental and Theoretical Investigation of Methane-Gas-Hydrate Dissociation in Porous Media. SPE Reservoir Engineering 6, 69-76.

Yu, P.-Y., Sean, W.-Y., Yeh, R.-Y., Chiang Hsieh, L.-H., Hsu, R.-Q., Sato, T., 2017. Direct numerical simulation of methane hydrate dissociation in pore-scale flow by using CFD method. International Journal of Heat and Mass Transfer 113, 176-183.

Yu, Y.-S., Zhang, X., Liu, J.-W., Lee, Y., Li, X.-S., 2021. Natural gas hydrate resources and hydrate technologies: a review and analysis of the associated energy and global warming challenges. Energy & Environmental Science 14, 5611-5668.

Yuan, Q., Sun, C., Yang, X., Ma, P., Ma, Z., Li, Q., Chen, G., 2011. Gas Production from Methane-Hydrate-Bearing Sands by Ethylene Glycol Injection Using a Three-Dimensional Reactor. Energy & Fuels 25, 3108-3115.

Zhang, L., Ge, K., Wang, J., Zhao, J., Song, Y., 2020. Pore-scale investigation of permeability

evolution during hydrate formation using a pore network model based on X-ray CT. Marine and Petroleum Geology 113, 104157.

Zhang, L., Kuang, Y., Zhang, X., Song, Y., Liu, Y., Zhao, J., 2017. Analyzing the Process of Gas Production from Methane Hydrate via Nitrogen Injection. Industrial & Engineering Chemistry Research 56, 7585-7592.

Zhang, L., Zhang, C., Zhang, K., Zhang, L., Yao, J., Sun, H., Yang, Y., 2019. Pore-Scale Investigation of Methane Hydrate Dissociation Using the Lattice Boltzmann Method. Water Resources Research 55, 8422-8444.

Zhao, J., Fan, Z., Wang, B., Dong, H., Liu, Y., Song, Y., 2016. Simulation of microwave stimulation for the production of gas from methane hydrate sediment. Applied Energy 168, 25-37.